PIEZOELECTRICS

An organic-inorganic perovskite ferroelectric with large piezoelectric response

Yu-Meng You,[1]*† Wei-Qiang Liao,[1]† Dewei Zhao,[2]† Heng-Yun Ye,[1] Yi Zhang,[1] Qionghua Zhou,[3] Xianghong Niu,[3] Jinlan Wang,[3] Peng-Fei Li,[1] Da-Wei Fu,[1] Zheming Wang,[4] Song Gao,[4] Kunlun Yang,[5] Jun-Ming Liu,[5] Jiangyu Li,[6,7]* Yanfa Yan,[2]* Ren-Gen Xiong[1]*

Molecular piezoelectrics are highly desirable for their easy and environment-friendly processing, light weight, low processing temperature, and mechanical flexibility. However, although 136 years have passed since the discovery in 1880 of the piezoelectric effect, molecular piezoelectrics with a piezoelectric coefficient d_{33} comparable with piezoceramics such as barium titanate (BTO; ~190 picocoulombs per newton) have not been found. We show that trimethylchloromethyl ammonium trichloromanganese(II), an organic-inorganic perovskite ferroelectric crystal processed from aqueous solution, has a large d_{33} of 185 picocoulombs per newton and a high phase-transition temperature of 406 kelvin (K) (16 K above that of BTO). This makes it a competitive candidate for medical, micromechanical, and biomechanical applications.

Piezoelectricity arises in crystalline materials without inversion symmetry, allowing interconversion between electric voltage and mechanical stress. This property makes piezoelectrics essential for high-voltage sources, sensors, actuators, frequency standard, motors, vibration reducer, and other applications. Pierre Curie and Jacques Curie were brothers who discovered piezoelectricity in 1880 (*1*). The Curies used tourmaline, quartz, topaz, cane sugar, and Rochelle salt to demonstrate the electromechanical interactions. Those first few piezoelectric materials have very weak piezoelectric performance, with piezoelectric coefficients of d_{33} < 10 pC/N (*2*). Among these piezoelectric materials, Rochelle salt is also a ferroelectric material, discovered in 1920 by Valasek (*3*). Ferroelectrics feature a switchable spontaneous electric polarization and usually also have good piezoelectric performance. The most widely used piezoelectric materials currently are ferroelectric ceramics such as lead zirconate titanate (PZT) and barium titanate (BTO), which have excellent electromechanical conversion and strong spontaneous polarization.

Piezoelectric materials should be thin, soft, lightweight, flexible, and also bio-friendly for a wide variety of important applications, such as microrobotics, flexible/wearable devices, and bioimplanted sensors (*4*–*6*). These requirements impose challenges for conventional piezoelectric ceramics, which require high processing temperatures, have almost no mechanical flexibility, and contain potential toxic elements. Because these problems can potentially be solved with organic materials, organic ferroelectrics have received intensive attention (*7*–*9*). Although researchers focus on improving the spontaneous polarization (P_s) and the phase-transition temperature (T_c) (*10*–*13*) of organic ferroelectrics, the piezoresponse of organic materials still do not match that of piezoceramics such as BTO. In our previous work, we reported the largest bulk d_{33} among molecular ferroelectrics in imidazolium perchlorate (41 pC/N), yet it is only one-fifth of that of single-crystal BTO (d_{33} = 90 and 190 pC/N along [001] and [111] crystal orientation, respectively) (*14*, *15*). Imidazolium perchlorate has an even smaller d_{33} than that of binary solid solutions such as PZT, which are as high as thousands of picocoulombs per newton with proper doping and phase engineering (*5*). Other organic materials have even weaker d_{33}, with ~20 pC/N for polyvinylidene fluoride (PVDF), 2 pC/N for nylon, 11 pC/N for diisopropylammonium bromide (DIPAB), and 5 pC/N for croconic acid.

Recent developments show the potential applications of organic-inorganic perovskite materials in electronics (*16*), light sources (*17*), photovoltaics (*18*, *19*), and even ferroelectrics (*20*). Because of their distinct structure, hybrid materials combine the benefits of organic molecules and advantageous characteristics of crystalline inorganic solids at a molecular level. We report the discovery of a single-phase organic-inorganic perovskite piezoelectric of trimethylchloromethyl ammonium trichloromanganese(II) [$Me_3NCH_2ClMnCl_3$, (TMCM-$MnCl_3$)] that exhibits a piezoelectric coefficient

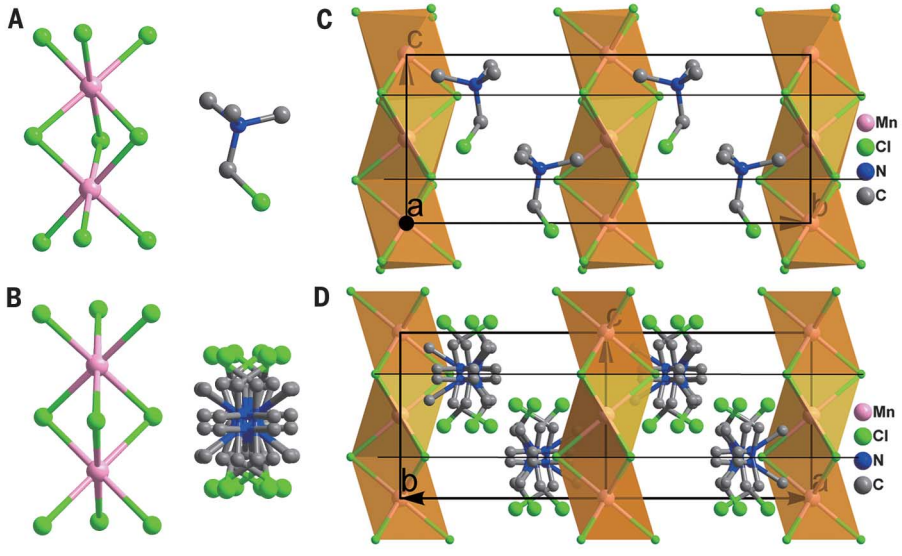


Fig. 1. Thermal variation of crystal structures of TMCM-$MnCl_3$. (**A**) Structural unit of TMCM-$MnCl_3$ in the LTP, showing the coordination geometry of the $MnCl_6$ octahedron and cationic structure. (**B**) Structural unit of TMCM-$MnCl_3$ in the HTP, showing the multi-orientation of the cation. (**C**) Projection of the low-temperature structure. The dark lines indicate the pseudo–mirror planes normal to the *c* axis, which illustrate the relative ionic displacement due to symmetry-breaking. (**D**) Projection of the high-temperature structure. The dark lines indicate the mirror planes normal to the *a* axis. H atoms were omitted for clarity.

[1]Ordered Matter Science Research Center, Southeast University, Nanjing, Jiangsu 211189, P. R. China. [2]Department of Physics and Astronomy, University of Toledo, Toledo, OH 43606, USA. [3]Department of Physics, Southeast University, Nanjing, Jiangsu 211189, P. R. China. [4]College of Chemistry and Molecular Engineering, Peking University, Beijing 100871, P. R. China. [5]Laboratory of Solid State Microstructures and Innovation Center of Advanced Microstructures, Nanjing University, Nanjing 210093, P. R. China. [6]Shenzhen Key Laboratory of Nanobiomechanics, Shenzhen Institutes of Advanced Technology, Chinese Academy of Sciences, Shenzhen, Guangdong 518055, P. R. China. [7]Department of Mechanical Engineering, University of Washington, Seattle, WA 98195-2600, USA.
***Corresponding author. Email: youyumeng@seu.edu.cn (Y.-Y.M.); jjli@u.washington.edu (J.L.); yanfa.yan@utoledo.edu (Y.Y.); xiongrg@seu.edu.cn (R.-G.X.)**
†These authors contributed equally to this work.

Downloaded from http://science.sciencemag.org/ on July 20, 2017

d_{33} of 185 pC/N. Such a large d_{33} makes TMCM-$MnCl_3$ a molecular material with a piezoelectric coefficient comparable with that of piezoelectric ceramics such as $BaTiO_3$. TMCM-$MnCl_3$ is also a high-temperature molecular ferroelectric with a T_c of 406 K (16 K above that of BTO), making it attractive for practical applications. Unlike inorganic piezoceramics, which require high-temperature synthesis and a high-voltage poling process before applications, TMCM-$MnCl_3$ is synthesized at room temperature with a preferential macroscopic ferroelectric polarization, making it suitable for growing on low-melting-point flexible substrates and fully compatible with solution-based large-area fabrication techniques. Moreover, the toxic-metal–free composition suggests that TMCM-$MnCl_3$ may be a great candidate for next-generation micro-electromechanical systems (MEMS), flexible devices, wearable devices, medical implants, and nanogenerators.

We prepared large crystals of TMCM-$MnCl_3$ in aqueous solution at room temperature (*2*) (figs. S1 and S2). We determined the structure with x-ray diffraction (XRD) at different temperatures (Fig. 1 and table S1). The low-temperature phase (LTP) of TMCM-$MnCl_3$ obtained at room temperature belongs to the polar space group *Cc* (*2*). The crystal packing adopts the $BaNiO_3$-like perovskite structure, similar to several other molecular ferroelectrics (*21*). The Me_3NCH_2Cl cation is derived from the spherical tetramethylammonium cation by replacing a H atom with a Cl atom. Typically, three-dimensional molecules such as tetramethylammonium and damantane tend to exhibit dynamical disorder in close-packed crystals because of weak van der Waals interactions. As for TMCM-$MnCl_3$, the Cl atom disturbs the spherical symmetry and thus induces the potential energy barrier to its tumbling motion. The high-temperature phase (HTP) is centrosymmetric, with the space group $P6_3/mmc$. The relationship between the two lattice cells is $\mathbf{a}^{LTP} \approx -\mathbf{a}^{HTP} - \mathbf{b}^{HTP}$, $\mathbf{b}^{LTP} \approx \mathbf{a}^{HTP} - \mathbf{b}^{HTP}$, and $\mathbf{c}^{LTP} \approx \mathbf{c}^{HTP}$ (Fig. 1A). We modeled the molecular tumbling with 12-fold orientational disorder (fig. S2). We found that in the HTP, only the N atom can be located from the difference Fourier map, indicating a strong dynamic characteristic of the molecular tumbling.

From the crystal structures of HTP and LTP, the phase-transition between these phases is induced by the order-disorder transition of the cations. In the paraelectric HTP, the crystal has a centrosymmetric structure because of the dynamic disorder of the organic cation. In the ferroelectric LTP, the crystal loses centrosymmetry because of the "freeze" of cations, which leads to the spontaneous polarization. We measured the temperature-dependent second-harmonic generation (SHG) response that supports the breaking of centrosymmetry (fig. S3). According to Aizu, this phase-transition of 6/*mmm*Fm (Aizu notation) is one of the 88 species of ferroelectrics (*22*). We confirmed the ferroelectricity by observing the typical polarization-electric field (*P*–*E*) hysteresis loops using the double-wave method (Fig. 2A) (*23*) and the Sawyer-Tower method (fig. S4).

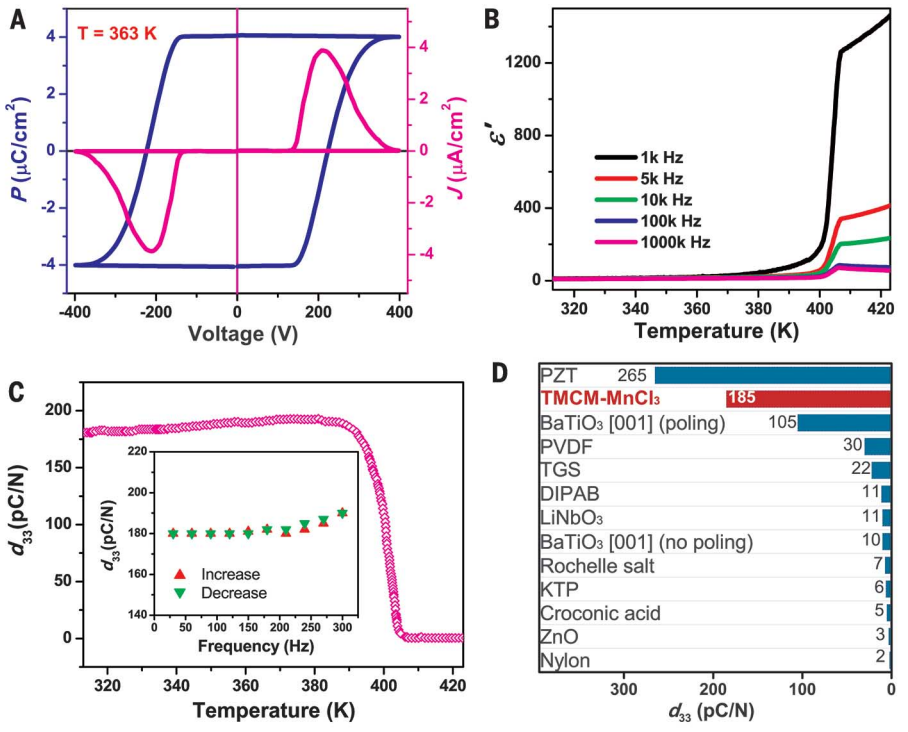


Fig. 2. Ferroelectric and related properties of TMCM-$MnCl_3$. (**A**) Current density-bias voltage (*J*~*V*) curves and polarization-bias voltage (*P*~*V*) hysteresis loop. (**B**) Temperature-dependent data of the real part (ε′) of dielectric permittivity (ε = ε′ − *i*ε″, where ε″ is imaginary part of ε). (**C**) Piezoelectric coefficient (d_{33}) of TMCM-$MnCl_3$ as a function of temperature and (inset) frequency. (**D**) Piezoelectric coefficient of TMCM-$MnCl_3$ compared with some inorganic and molecular materials, including PZT, BTO, PVDF, ZnO, $LiNbO_3$, Nylon, Rochelle salt, potassium titanyl phosphate (KTP), triglycine sulfate (TGS), DIPAB (*10*), $ImClO_4$ (*26*), and croconic acid (*12*). Measured d_{33} values are listed at the end of each bars.

We measured the saturate polarization (P_s) of 4.0 μC/cm^2 with both methods, which corresponded well with the calculated theoretical results (fig. S5) (*2*). Such a polarization value is in the intermediate range among reported molecule-based ferroelectrics (*9*, *24*). We subjected a crystal of TMCM-$MnCl_3$ to polarization switching for up to 10^7 cycles, and it showed fatigue of <10% (fig. S6).

Steplike dielectric anomalies reveal the improper ferroelectric character of the transition (Fig. 2B). We obtained a phase-transition temperature of T_c = 406 K, which is consistent with the results from several temperature-dependent measurements (fig. S3). In such an improper ferroelectric compound, the Curie-Weiss law is not applicable (*25*). We also measured the frequency-dependent dielectric permittivity and the imaginary part of the dielectric permittivity (figs. S8 and S9). A simple model described by the Landau-Ginzburg theory can be applied to explain the behavior of dielectric permittivity around T_c (fig. S7) (*2*).

Ferroelectrics are naturally piezoelectrics because of the lack of an inversion center, but most organic materials have a very weak piezoelectric response. As one of the elements in the matrix of direct piezoelectric coefficient, d_{33} represents the ability of a material to generate charges on the plane normal to the applied strain (eqs. S1 and S2) (*2*). Because inorganic ferroelectrics are normally grown in the high-temperature paraelectric phase, they exhibit multidomain structures and require high-voltage poling processing before their application. Unlike inorganic ferroelectrics, crystals of TMCM-$MnCl_3$ are grown at room temperature and exhibit a nice monodomain structure (fig. S10). To measure d_{33}, we used a quasi-static method (also known as the Berlincourt method) on the as-grown single-crystal of TMCM-$MnCl_3$. In the temperature-dependent study, we obtained a maximum d_{33} of 185 pC/N along the proximity of the [102] direction of the crystal in the LTP. For temperatures above T_c, d_{33} vanishes because of the restoration of centrosymmetry, which corresponds very well with the SHG data. We also tested the piezoresponse of TMCM-$MnCl_3$ with the frequency of driving force varying from 30 to 300 Hz (Fig. 2C, inset), and this shows very little fluctuation (<10 pC/N). For a direct comparison, we measured piezoelectric coefficients of a few piezoelectric materials and several molecular ferroelectrics under the same experimental conditions (Fig. 2D and table S2). The results show that as a mono-composition ferroelectric, TMCM-$MnCl_3$ exhibits an abnormally large piezoelectric coefficient among undoped metal oxides and other molecular materials (*26*).

Downloaded from http://science.sciencemag.org/ on July 20, 2017

Both intrinsic and extrinsic factors contribute to the piezoelectricity. The intrinsic piezoresponse raises from the polarization change because of the lattice distortion, whereas the extrinsic factors are normally caused by the movement of non-180° domain walls or interaction between crystal grains (*27*). Because we obtained the macroscopic d_{33} on the as-grown single-crystalline monodomain sample, we expected the large d_{33} to be intrinsic. To further confirm the large d_{33}, we used a piezoresponse force microscopy (PFM) technique, whose submicrometer spatial resolution allows us to probe the piezoresponse within a single domain (*28*–*31*). With the sample heated up and then cooled down from the HTP paraelectric phase, the polydomain state can be obtained (figs. S11 to S15) (*2*). The typical PFM phase and amplitude images are shown in Fig. 3, A and B, respectively. The surface appeared as a beautiful lamellar multidomain structure. The local piezoresponse was then obtained on one of the single domains via extraction from the piezoresponse amplitude spectrum as a function of DC bias voltage, also known as a "butterfly" curve (Fig. 3C, inset, and fig. S11) (*32*). Such local piezoresponses obtained from $LiNbO_3$, triglycine sulfate (TGS), BTO, and TMCM-$MnCl_3$ were plotted as a function of macroscopic d_{33} measured with the Berlincourt method (Fig. 3C). A good linear relationship was observed. Because the local piezoresponse is proportional to the macroscopic d_{33}, the prefactor for the dependence is related to the tip-sample geometry and other factors (*29*), which are not in the scope of this work. From these local microscopic measurements, the observed large d_{33} on TMCM-$MnCl_3$ can be well supported.

To explain the origin of such a large d_{33}, we need to understand the structural properties of TMCM-$MnCl_3$. In the binary system of PZT, which is a solid solution of $PbZrO_3$ and $PbTiO_3$, a maximum d_{33} > 220 pC/N can be obtained at Zr/Ti = 0.52/0.48 by changing the relative composition of Zr. The large d_{33} is attributed to the morphotropic phase boundary between tetragonal and rhombohedral phases (*33*). For the single-composition crystal of TMCM-$MnCl_3$, the large d_{33} is due to the organic-inorganic structure. Whereas the space group of the HTP of TMCM-$MnCl_3$ is $P6_3/mmc$, the space group of LTP of TMCM-$MnCl_3$ is the nonmaximal subgroup Cc. In this case, compared with the HTP, TMCM-$MnCl_3$ loses more than one symmetry elements in the ferroelectric LTP, leading to the multipolar-axes characteristic, which is supported by the observation of lamellar domain structures and non-180° domain walls (Fig. 3, A and B). From crystallographic analysis and vector-PFM analysis (figs. S12 to S14) (*2*), there are six polar axes in TMCM-$MnCl_3$, resulting in 12 different polarization directions (Fig. 3D, inset). Moreover, by examining the strain tensors in the LTP, TMCM-$MnCl_3$ is also a partially ferroelastic material (*2*, *22*, *34*). Polarization states on the same polar axis, P_i^+ and P_i^- (i = 1, 2,..., 6), belong to the same strain state S_i (i = 1, 2,..., 6). Under an external stress, materials with ferroelasticity switch from one strain state to the other, which has been intensively studied in inorganic ferroelectrics, such as BTO and PZT (*35*). In our case, when the external stress switches TMCM-$MnCl_3$ from S_i to S_j (i, j = 1, 2,..., 6), the polarization state is also switched from $P_i^{+/-}$ to $P_j^{+/-}$ (i, j = 1, 2,..., 6), respectively. Such rotation of polarization direction prompts an anomalously large change of the polarization, leading to the large piezoresponsivity.

Moreover, TMCM-$MnCl_3$ displays excellent photoluminescence properties, with a near-unity photoluminescence emission efficiency (figs. S16 to S18) (*2*). A thin-film sample of TMCM-$MnCl_3$ can also be prepared with large-area coverage and good uniformity by means of a simple drop-cast method (fig. S19). The PFM characterization on domain structure and polarization reversal have also been carried out on thin-film of TMCM-$MnCl_3$ (figs. S20 to S23) (*2*). Because the large piezoelectricity is due to the particular structural property, more piezoelectrics may be formed by replacing Mn with other metals. For example, we synthesized a high-temperature molecular piezoelectric compound of trimethylchloromethyl ammonium trichlorocadmium(II) [$Me_3NCH_2ClCdCl_3$ (TMCM-$CdCl_3$)] that has similarly attractive piezoelectric properties (figs. S24 to S27) (*2*).

We have discovered an organic-inorganic perovskite ferroelectric material of $Me_3NCH_2ClMnCl_3$ (TMCM-$MnCl_3$) that shows an excellent piezoelectric response (d_{33} = 185 pC/N) that is close to that of inorganic piezoelectrics of BTO (d_{33} = 190 pC/N) and a high transition temperature T_c of 406 K. The room-temperature process avoids the high-temperature sintering and high-voltage poling process. Solution-based processing allows deposition of TMCM-$MnCl_3$ on various substrates, including flexible polymer, making it attractive for a variety of applications. Moreover, TMCM-$MnCl_3$ is an organic-inorganic material that can be further engineered through element substitution and molecular design so as to optimize for a desired physical property, as shown by demonstrations of bandgap engineering (*20*). Combining the outstanding piezoelectric properties and application advantages of molecular materials, we believe that this class of material has great potential for the next generation of MEMS, flexible devices, wearable devices, and bionics.

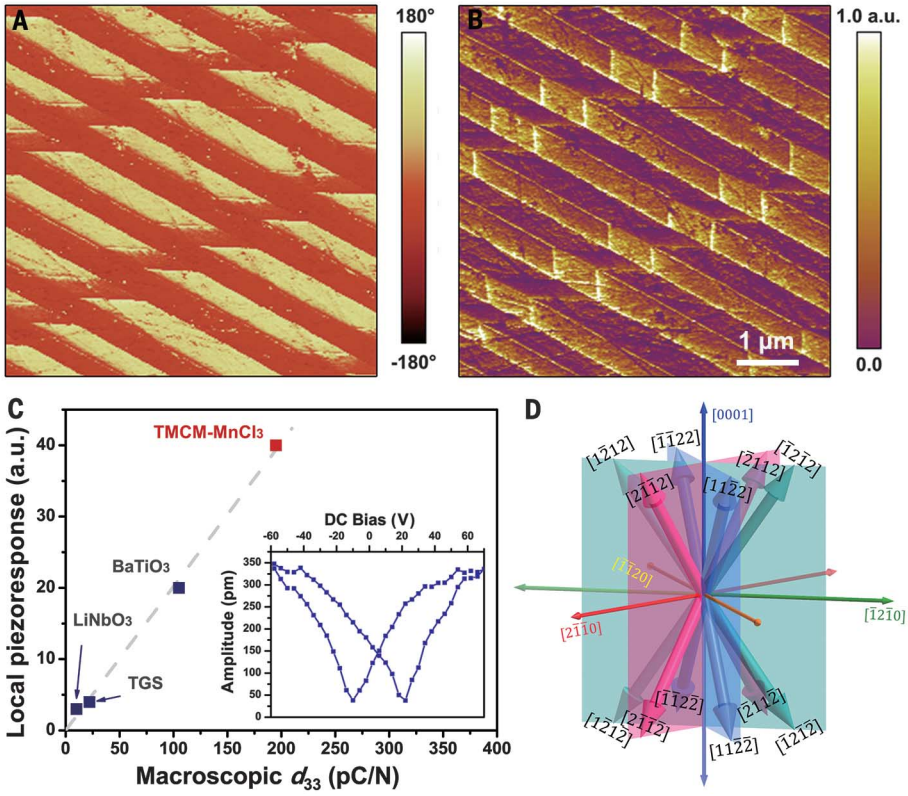


Fig. 3. Microscopic ferroelectric/piezoelectric properties of TMCM-$MnCl_3$. (**A** and **B**) Ferroelectric domain structures seen in PFM images constructed by (A) phase and (B) amplitude signal of the out-of-plane piezoresponse, where the non-180° domain structure can be clearly observed, indicating the multipolar-axes feature. (**C**) Comparison of local piezoresponse measured with PFM. The data are plotted against macroscopic d_{33} so as to demonstrate the linear dependence. (Inset) The local piezoresponse of TMCM-$MnCl_3$ as a function of DC bias voltage. (**D**) Illustration of the 12 different polarization directions.

REFERENCES AND NOTES

1. J. Curie, P. Curie, *C. R. Acad. Sci. Paris* **91**, 294–297 (1880).
2. Materials, methods, and supplementary text are available as supplementary materials.
3. J. Valasek, *Phys. Rev.* **17**, 475–481 (1921).

Downloaded from http://science.sciencemag.org/ on July 20, 2017

4. J. Rödel *et al*., *J. Am. Ceram. Soc.* **92**, 1153–1177 (2009).
5. Y. Saito *et al*., *Nature* **432**, 84–87 (2004).
6. Z. L. Wang, J. Song, *Science* **312**, 242–246 (2006).
7. T. Akutagawa *et al*., *Nat. Mater.* **8**, 342–347 (2009).
8. B. Xu, S. Ren, *Small* **12**, 4502–4507 (2016).
9. P.-P. Shi *et al*., *Chem. Soc. Rev.* **45**, 3811–3827 (2016).
10. D. W. Fu *et al*., *Science* **339**, 425–428 (2013).
11. A. S. Tayi *et al*., *Nature* **488**, 485–489 (2012).
12. S. Horiuchi *et al*., *Nature* **463**, 789–792 (2010).
13. D. A. Bonnell, *Science* **339**, 401–402 (2013).
14. R. Bechmann, *J. Acoust. Soc. Am.* **28**, 347–350 (1956).
15. S. Wada, K. Yako, H. Kakemoto, T. Tsurumi, T. Kiguchi, *J. Appl. Phys.* **98**, 014109 (2005).
16. D. B. Mitzi, C. A. Feild, W. T. A. Harrison, A. M. Guloy, *Nature* **369**, 467–469 (1994).
17. H. Cho *et al*., *Science* **350**, 1222–1225 (2015).
18. F. Hao, C. C. Stoumpos, D. H. Cao, R. P. H. Chang, M. G. Kanatzidis, *Nat. Photonics* **8**, 489–494 (2014).
19. H. Tsai *et al*., *Nature* **536**, 312–316 (2016).
20. H.-Y. Ye *et al*., *Adv. Mater.* **28**, 2579–2586 (2016).
21. H.-Y. Ye *et al*., *J. Am. Chem. Soc.* **137**, 13148–13154 (2015).
22. K. Aizu, *J. Phys. Soc. Jpn.* **27**, 387–396 (1969).
23. L. Hu, S. Dalgleish, M. M. Matsushita, H. Yoshikawa, K. Awaga, *Nat. Commun.* **5**, 3279 (2014).
24. W. Zhang, R.-G. Xiong, *Chem. Rev.* **112**, 1163–1195 (2012).
25. A. P. Levanyuk, D. G. Sannikov, *Usp. Fiziol. Nauk* **112**, 561–589 (1974).
26. Y. Zhang *et al*., *Angew. Chem. Int. Ed.* **53**, 5064–5068 (2014).
27. D. Damjanovic, *Rep. Prog. Phys.* **61**, 1267–1324 (1998).
28. D. A. Bonnell, S. V. Kalinin, A. Kholkin, A. Gruverman, *MRS Bull.* **34**, 648–657 (2009).
29. A. L. Kholkin, S. V. Kalinin, A. Roelofs, A. Gruverman, in *Scanning Probe Microscopy: Electrical and Electromechanical Phenomena at the Nanoscale*, S. Kalinin, A. Gruverman, Eds. (Springer New York, 2007), pp. 173–214.
30. H. Lu *et al*., *Adv. Mater.* **27**, 7832–7838 (2015).
31. D. A. Bonnell *et al*., *Rev. Mod. Phys.* **84**, 1343–1381 (2012).
32. M. E. Caspari, W. J. Merz, *Phys. Rev.* **80**, 1082–1089 (1950).
33. W. Heywang, K. Lubitz, W. Wersing, *Piezoelectricity: Evolution and Future of a Technology* (Springer, 2008).
34. N. Setter, E. L. Colla, *Ferroelectric Ceramics: Tutorial Reviews, Theory, Processing, and Applications* (Birkhauser, 1993).
35. J. L. Jones, M. Hoffman, J. E. Daniels, A. J. Studer, *Physica B* **385–386**, 100–102 (2006).

ACKNOWLEDGMENTS

The manuscript was improved by the insightful reviews by the anonymous reviewers. This work was supported by the 973 project (grant 2014CB932103), the National Natural Science Foundation of China (grants 21290172, 91422301, 21427801, and 21290170), and the National Key Research Program of China (grants 2016YF0300101 and 2016YFA0201001). The d_{33} data reported in this paper are tabulated in the supplementary materials. Data of crystal structures reported in this paper are deposited at the Cambridge Crystallographic Data Centre (deposition nos. CCDC 1429417-1429418 and 1515805-1515806).

SUPPLEMENTARY MATERIALS

www.sciencemag.org/content/357/6348/306/suppl/DC1
Materials and Methods
Supplementary Text
Figs. S1 to S27
Tables S1 to S3
References (*36*–*68*)

22 August 2016; resubmitted 21 December 2016
Accepted 19 June 2017
10.1126/science.aai8535

Downloaded from http://science.sciencemag.org/ on July 20, 2017

Science

An organic-inorganic perovskite ferroelectric with large piezoelectric response

Yu-Meng You, Wei-Qiang Liao, Dewei Zhao, Heng-Yun Ye, Yi Zhang, Qionghua Zhou, Xianghong Niu, Jinlan Wang, Peng-Fei Li, Da-Wei Fu, Zheming Wang, Song Gao, Kunlun Yang, Jun-Ming Liu, Jiangyu Li, Yanfa Yan and Ren-Gen Xiong

Science **357** (6348), 306-309.
DOI: 10.1126/science.aai8535

Finding a more flexible mechanical sensor

Piezoelectric materials allow conversion between electricity and mechanical stresses. The most efficient piezoelectric materials are ceramics such as $BaTiO_3$ or $PbZrO_3$, which are also extremely stiff. You *et al.* identified an organic perovskite structured piezoelectric material that is far more pliable yet has a piezoelectric response similar to that of traditional ceramics. This material may be a better option to use as a mechanical sensor for flexible devices, soft robotics, biomedical devices, and other micromechanical applications that benefit from a less stiff piezoelectric material.

Science, this issue p. 306

ARTICLE TOOLS http://science.sciencemag.org/content/357/6348/306

SUPPLEMENTARY MATERIALS http://science.sciencemag.org/content/suppl/2017/07/20/357.6348.306.DC1

REFERENCES This article cites 64 articles, 4 of which you can access for free
http://science.sciencemag.org/content/357/6348/306#BIBL

PERMISSIONS http://www.sciencemag.org/help/reprints-and-permissions

Use of this article is subject to the Terms of Service

Science (print ISSN 0036-8075; online ISSN 1095-9203) is published by the American Association for the Advancement of Science, 1200 New York Avenue NW, Washington, DC 20005. 2017 © The Authors, some rights reserved; exclusive licensee American Association for the Advancement of Science. No claim to original U.S. Government Works. The title *Science* is a registered trademark of AAAS.

Downloaded from http://science.sciencemag.org/ on July 20, 2017

www.sciencemag.org/content/357/6348/306/suppl/DC1

Supplementary Material for

An organic-inorganic perovskite ferroelectric with large piezoelectric response

Yu-Meng You,* Wei-Qiang Liao, Dewei Zhao, Heng-Yun Ye, Yi Zhang, Qionghua Zhou, Xianghong Niu, Jinlan Wang, Peng-Fei Li, Da-Wei Fu, Zheming Wang, Song Gao, Kunlun Yang, Jun-Ming Liu, Jiangyu Li,* Yanfa Yan,* Ren-Gen Xiong*

*Corresponding author. Email: youyumeng@seu.edu.cn (Y.-Y.M.); jjli@u.washington.edu (J.L.); yanfa.yan@utoledo.edu (Y.Y.); xiongrg@seu.edu.cn (R.-G.X.)

Published 21 July 2017, *Science* **357**, 306 (2017)
DOI: 10.1126/science.aai8535

This PDF file includes:

Materials and Methods
Supplementary Text
Figs. S1 to S27
Tables S1 to S3
References

Materials and Methods

Crystal growth

(Chloromethyl)trimethylammonium chloride was synthesized by the reaction of equimolar amounts of trimethylamine (30 wt % in water) and dichloromethane in acetonitrile at room temperature for 24 h. The solvent was removed under reduced pressure. The obtained colorless solid is hygroscopic and should be stored in a vacuum desiccator. Slow evaporation of a methanol solution (100 ml) of (chloromethyl)trimethylammonium chloride (50 mmol) and anhydrous manganese(II) chloride (50 mmol) resulted in the formation of red block single crystals of $Me_3NCH_2ClMnCl_3$ (TMCM-$MnCl_3$). The purity of the bulk phase was verified the powder X-ray diffraction (Fig. S1).

Characterization Methods

Common characterization methods like differential scanning calorimetry (DSC), second harmonic generation (SHG) and photoluminescence spectroscopy measurements were described elsewhere (*26, 36, 37*). In these measurement, powder sample were used.

The macroscopic piezoelectric coefficient (d_{33}) was measured by a commercial piezometer (Piezotest, model: PM200) using "Berlincourt" method (also called "quasi-static" method). The sample crystal was placed in between two flat metal plates which clamp the sample and apply a small oscillating force (5 N) along the normal direction, while the piezoelectric charge is measured. The Berlincourt method is a simple and straightforward way to measure the direct piezoelectric coefficient, d_{33}. All measured crystals were selected with defined shape and the aspect ratio is more than 3 to ensure the d_{33} is correctly measured. The maximum of d_{33} value was found along the polar-axis of the sample crystal, which is near the proximity of <102> direction.

For macroscopic ferroelectric test, a bulk crystal with thickness of ~0.3 mm was used with conducting silver-paste served as top and bottom electrodes. Two methods were employed to examine the ferroelectric properties: Sawyer-Tower method and double-wave method(*23*). The Sawyer-Tower method was carried out on a commercial equipment (Radiant Tech. Inc. Model: Premier II) with operation frequency of 50 Hz. The double-wave method was carried out on a home-built system consisting of programmable waveform generator (Agilent, Model: 33521A), high-voltage amplifier (Trek, Model: 623B) and programmable low-current electrometer (Keithley, Model: 6514).

The sample for dielectric permittivity measurement was similar bulk crystal used for ferroelectric test with conducting silver-paste served as top and bottom electrodes. The dielectric permittivity (ε) is measured on an “automatic component analyzer” (Tonghui Inc. Model: TH2828A) over the frequency range from 200 Hz to 1 MHz with AC voltage of 1 V.

The pyroelectric data was obtained on the same sample as ferroelectric test. A digital oven was used to control the sample temperature and a low-current electrometer (Keithley, Model: 6514) was used to record the pyroelectric current.

PFM characterizations

The PFM measurement was carried out on a commercial piezoresponse microscope (Oxford instrument, MFD-3D) with high-voltage package and in-situ heating stage. PFM is based on atomic force microscopy (AFM), with an AC drive voltage applied to the conductive tip. When the tip is in contact with the sample surface, the local piezoelectric response can be detected by recording the distortional motion of the cantilever. Thus the piezoresponse can be estimated measuring the vibrating amplitude of the cantilever per unit drive voltage. In Fig. 3C, the microscopic piezoresponse was calculated by dividing the maximum amplitude of in the inset by the drive voltage.

While the phase and amplitude of the electromechanical response of the surface reflect the orientation and magnitude of local ferroelectric polarization, respectively, image of local domain structure can be constructed by scanning the tip over sample surface, as shown in Fig. 3A and 3B. Furthermore, electromechanical response can also be probed as a function of DC bias of the tip, providing manipulations on the polarization directions.

Thin-film preparation

A methanol solution (20 μL) contains 40 mg/ml TMCM-$MnCl_3$ was dropped onto a clean ITO-glass substrate (1.5 × 1.5 cm). The substrate with the droplet was placed inside a sealed Petri dish (35 × 10 mm). High quality plate-shaped crystals formed on the ITO-glass substrate after the solvent slowly evaporated on a hot plate of 35 ± 1 °C.

Supplementary Text

In this manuscript, we used Voigt notation (d_{mn}, where m = 1, 2, 3, and n = 1,…,6) following ANSI IEEE 176 standard to represent the piezoelectric coefficient. But in fact the piezoelectric coefficient is actually a third rank tensor and its non-contracted form is d_{ijk} (i, j, k = 1, 2, 3).

Crystal data of TMCM-$MnCl_3$

At 293 K: $C_4H_{11}Cl_4MnN$, Mr = 269.88, monoclinic, Cc, a = 9.478(5), b = 15.741, c = 6.577(3) Å, V = 977.7(8) Å^3, Z = 4, D_c = 1.834 g cm^{-3}, μ = 2.375 mm^{-1}, R_1 ($I > 2\sigma(I)$) = 0.0216, wR_2 (all data) = 0.0465, S = 0.948.

At 423 K: $C_4H_{11}Cl_4MnN$, Mr = 269.88, hexagonal, $P6_3/mmc$, a = 9.523(5), c = 6.638(7) Å, V = 521.3(8) Å^3, Z = 2, D_c = 1.719 g cm^{-3}, μ = 2.227 mm^{-1}, R_1 ($I > 2\sigma(I)$) = 0.0868, wR_2 (all data) = 0.2434, S = 1.398.

Piezoelectric coefficient matrix

Considering the point group m of TMCM-$MnCl_3$ in its ferroelectric phase, based on ANSI IEEE 176, the piezoelectric constant matrix $[d]$ can be written as:

$$\begin{pmatrix} d_{11} & d_{12} & d_{13} & 0 & d_{15} & 0 \\ 0 & 0 & 0 & d_{24} & 0 & d_{26} \\ d_{31} & d_{32} & d_{33} & 0 & d_{35} & 0 \end{pmatrix} \quad \text{(S1)},$$

And the matrix $[d^T]$ of converse piezoelectric can be derived as:

$$\begin{pmatrix} d_{11} & 0 & d_{31} \\ d_{12} & 0 & d_{32} \\ d_{13} & 0 & d_{33} \\ 0 & d_{24} & 0 \\ d_{15} & 0 & d_{35} \\ 0 & d_{26} & 0 \end{pmatrix} \quad \text{(S2)}.$$

The element d_{33} is the longitudinal piezoelectric coefficient, which characterizes the volume change as response to an applied electric field in the same direction.

Symmetry analysis on the partial ferroelasticity

According to the symmetry change, the crystal of TMCM-$MnCl_3$ belongs to the 6/*mmm*F*m* species which is among the 31 fully-ferroelectric/partially ferroelastic species (*34*). The "fully-ferroelectric" means that by applying electric-field, in principle, one can access all possible ferroelectric domain states. The "partially ferroelastic" means that by only applying stress, one can not access all possible ferroelastic states.(*22*) TMCM-$MnCl_3$ has twelve ferroelectric states (different polarization directions), and each state of the ferroelectric crystal should have the mirror plane superimposed with (1 -1 0 0)-plane, or (0 1 -1 0)-plane, or (1 0 -1 0)-plane of the prototype. We set a rectangular coordinate system in the prototype of the 6/*mmm*, tacking the z-axis parallel to the six-fold axis, x-axis perpendicular to the (1 1 -2 0)-plane and z-axis perpendicular to the (1 -1 0 0)-plane. Suppose P_1^+ is in the *yz*-plane of the rectangular coordinate system. It can be found that any operations of point group 6/*mmm* keeps P_1^+ either unchanged or change to one of eleven different orientation states. By applying the symmetry operation of m_y, m_z or C_2x (the suffix x, y, and z indicate the directions of the symmetry elements, respectively) on P_1^+, the polarization states of P_2^+, P_2^- and P_1^-in the same plane can be generated. By applying of C_3 the symmetry operation on $P_1^{+/-}$ and $P_2^{+/-}$, other eight polarization states can be generated. To determine whether TMCM-$MnCl_3$ is ferroelastic, partially ferroelastic or non-ferroelastic, we examine the strain tensor of the twelve polarization states. In state P_1^+, the strain tensor has the form:

$$\begin{pmatrix} a & 0 & 0 \\ 0 & b & d \\ 0 & d & c \end{pmatrix} \quad \text{(S3)}$$

By applying the operation of m_y, m_z and C_2x to strain tensor (S3), one obtains the strain tensor (S4), (S5) and (S6) of P_2^+, P_2^- and P_1^-, respectively:

$$\begin{pmatrix} a & 0 & 0 \\ 0 & b & -d \\ 0 & -d & c \end{pmatrix} \quad \text{(S4)},$$

$$\begin{pmatrix} a & 0 & 0 \\ 0 & b & -d \\ 0 & -d & c \end{pmatrix} \quad \text{(S5)}$$

and

$$\begin{pmatrix} a & 0 & 0 \\ 0 & b & d \\ 0 & d & c \end{pmatrix} \quad \text{(S6)}.$$

From those strain tensors, one can conclude that P_1^+, P_1^- have the same strain state S_1, and P_2^+ and P_2^- have the same strain state S_2.

By applying the operation of C_3 to the strain tensor of $P_1^{+/-}$ and $P_2^{+/-}$, (S3) to (S6), one obtains eight strain tensors of $P_3^{+/-}$, $P_4^{+/-}$, $P_5^{+/-}$, $P_6^{+/-}$, among which, only four independent strain tensors can be obtained, as (S7), (S8), (S9) and (S10):

$$\begin{pmatrix} -b & b & -d \\ -b & -a+b & -d \\ d & -d & c \end{pmatrix} \quad \text{(S7)}$$

$$\begin{pmatrix} a-b & -a & d \\ a & -a & 0 \\ -d & d & c \end{pmatrix} \quad \text{(S8)}$$

$$\begin{pmatrix} -b & b & d \\ -b & -a+b & d \\ -d & d & c \end{pmatrix} \quad \text{(S9)}$$

$$\begin{pmatrix} a-b & -a & -d \\ a & -a & 0 \\ d & -d & c \end{pmatrix} \quad \text{(S10)}$$

Each stain tensor is shared by two different polarization states, P_i^+ and P_i^- (i = 1, 2,…, 6). As a result, we obtained six independent strain tensors for TMCM-$MnCl_3$, thus there are six different ferroelastic states (S_1 to S_6) corresponding to total twelve ferroelectric states. According to Aizu's rule, TMCM-$MnCl_3$ belong to type (II) of the ferroelectric-ferroelastic crystals, i.e. fully ferroelectric and partially ferroelastic, similar to that of $BaTiO_3$ (*22*). For crystal of type (II), the different ferroelastic state can be switched by mechanical stress, which are accompanied by the change of polarization directions. In TMCM-$MnCl_3$, the polarization states with opposite direction have the same ferroelastic state, indicating that the mechanical stress can not reverse the polarization vector by 180º. But it is possible for external stress to rotate the polarization vector by non-180º. Such stress induced polarization switching is similar to that in BTO and PZT (*35, 38, 39*).

Local domain structure analyzed by PFM

In general, PFM can measure both the out-of-plane component (OP-PFM) and the in-plane component (IP-PFM) of the local piezoresponse by monitoring the vertical displacement and torsional movements of the cantilever, respectively. In Fig.

3, images were generated by OP-PFM which reveal the existence of non-180^{o} domain structures, which further supports the multi-polar-axes nature of TMCM-$MnCl_3$. In order to analyze the local domain structure and identify different polarization states, we have carried out comprehensive PFM studies on the surface of crystal of TMCM-$MnCl_3$, which include both OP-PFM and IP-PFM with different tip-sample orientation to extract information about the exact direction of polarization at different domains.

Since crystals of TMCM-$MnCl_3$ was grown in its ferroelectric phase and the growth temperature (~300 K) is much lower than the Curie temperature (406 K), the as-grown crystal of TMCM-$MnCl_3$ is in mono-domain state, as indicated by large area PFM images in Fig. S10. In order for TMCM-$MnCl_3$ to reach a poly-domain state, the crystal was heated up to its paraelectric phase and cooled down to its ferroelectric phase. PFM studies were then carried out with scan size of 50 × 50 μm, as shown in Fig. S12. Since the IP-PFM signal measures component of piezoresponse perpendicular to the cantilever-axis, in order to obtain the exact in-plane direction of the polarization, two sets of IP-PFM images were recorded with different cantilever-sample orientations, where the cantilever-sample orientations are indicated in the top left corner of Fig. S12A and S12B. In this way, we can obtain the in-plane component (*x*- and *y*-direction) and out-of-plane (*z*-direction) component of local piezoresponse. From the large-area PFM phase and amplitude images, complex domain structures can be observed. Irregular shaped super-domains (illustrated by different color contrast in Fig. S12D) consisting lamellar shaped sub-domains can be found in the phase images. Each super-domain has the same out-of-plane polarization direction and across the boundary of super-domains, all sub-domains reverse their polarization directions by ~180^{o} in both *x*-, *y*- and *z*-directions, indicated by corresponding phase images (Fig. S12A, S12B and S12C, respectively). By carefully studying the PFM images, two different sub-domain structures can be found in the examined area. To analyze the polarization direction of domain fine structures, high spatial resolution OP-PFM and IP-PFM were carried out in two areas with different sub-domain structures in similar super-domain, as indicated by the dotted blue box and green box.

With comprehensive phase and amplitude information in *x*-, *y*- and *z*-direction, one can obtain the sign (from phase images) and magnitude (from amplitude images) of polarization in each direction. In principle, by adding those vectors together, the exact polarization vector of each domain can be extracted. However, since OP-PFM and IP-PFM depend on different cantilever distortion, their absolute amplitudes are not comparable. Take the green boxed area as an example (Fig. S13A-J). The in-plane polarization directions for different types of domains with distinct polarization directions can be concluded (details can be found in the figure caption of Fig. S13). The out-of-plane polarization in this super-domain area was downward. By combining the results in green and blue boxed areas in Fig. S13, totally six in-plane polarization directions can be identified, with their out-of-plane polarization directions pointing downward. Considering the 180^{o} reversed super-domains, there are twelve different polarization directions found on the sample surface, as illustrated in Fig. S14, where solid (dashed) arrows indicate upward (downward) out-of-plane

polarization, respectively. Since we are not able to obtain the exact polarization directions in three-dimension, we can not compare the polarization directions in Fig. S14 with those indicated by crystal structure analysis as indicated in Fig. 3D. But the vector PFM results correspond well with previous discussion about multi-polar-axis, and the number of polarization states of TMCM-$MnCl_3$.

To further demonstrate the polarization reversal process in a more direct way, a DC bias voltage was applied on the conductive PFM tip while the tip was scanning over certain area of the sample surface. With such a strong local electric-field, local polarization directions can be manipulated, as shown in Figs. S15.

Theoretical calculation on ferroelectric polarization

The crystal polarization was further evaluated by the Berry phase method developed by King-Smith and Vanderbilt (*40, 41*) . We performed first-principle calculations within the framework of density functional theory (DFT) implemented in the Vienna *ab initio* Simulation Package (VASP) (*42, 43*). The exchange-correlation interactions were treated within the generalized gradient approximation of the Perdew-Burke-Ernzerh of type (*44*). The van de Waals interactions are considered by using DFT-D2 method of Grimme (*45*). For the purpose of comparison, we also included polarization calculated with other vdW corrections, as listed in Table S3. The ground state at room temperature was found to be antiferromagnetic along the $MnCl_3$ chain with a magnetic moment of 4.4 μB for each Mn atoms, which is 0.13 eV per unit cell lower than the ferromagnetic state. The calculated polarization vector lies in the *ac* plane. The vector module is 5.74 $\mu C/cm^2$ and its projection along the *c* direction is 4.48 $\mu C/cm^2$, which is close to the experimental value. Then we allowed the atoms to relax until atomic forces on each atom are smaller than 0.002 eV/Å. The polarization of this optimized structure is about 4.92 $\mu C/cm^2$ in the *c* direction, which gives an expectation of larger polarization at lower temperatures. The continuous evolution of spontaneous polarization (both module and projection in the *c* direction) from the centrosymmetric structure ($\lambda = 0$) to the optimized polar structure ($\lambda = 1$) is plotted as a function of dimensionless parameter λ in Fig. S5. Both the displacement and the rotation of the $(CH_3)_3NCH_2Cl$ cations are included in λ.

Model for fitting the temperature dependent real part of dielectric permittivity (ε)

The dielectric permittivity ε as a function of temperature T across the improper ferroelectric phase transition point T_C is described by the Landau-Ginzburg theory proposed earlier (*46-48*). The Landau energy density f is written as:

$$f = \frac{1}{2}\alpha(T - T_0)\eta^2 + \frac{1}{4}\beta\eta^4 + \frac{1}{6}\gamma\eta^6 + \frac{1}{2}\varepsilon_0^{-1}P^2 + a_1\eta^2 P + a_2\eta^2 P^2 - EP \quad \text{(S11)}$$

where ($\alpha > 0$, β, $\gamma > 0$, $\varepsilon_0 > 0$, a_1, $a_2 > 0$) are the free energy constants in the polynomials, T_0 is the unstable limit of high-temperature paraelectric phase, η is the

primary order parameter and *P* is the spontaneous polarization as the secondary order parameter, *E* is the electric field.

To determine the temperature dependences of $P(T)$ and $\eta(T)$, it is necessary to find the minimum of the Landau energy *f* with $E = 0$. The polarization *P* can be obtained from the following equilibrium conditions for both paraelectric phase and ferroelectric phase:

$$\frac{\partial f}{\partial \eta} = \alpha(T - T_0)\eta + \beta\eta^3 + \gamma\eta^5 + 2a_1\eta P + 2a_2\eta P^2 = 0 \quad ,$$

(S12)

and

$$\frac{\partial f}{\partial P} = \chi_0^{-1} P + a_1\eta^2 + 2a_2\eta^2 P = 0 \quad ,$$

(S13)

In the high-temperature paraelectric phase, $P = 0$, $\eta = 0$, and $\varepsilon = \varepsilon_0$ which is a constant. This implies that the dielectric permittivity in the paraelectric phase is temperature-independent. For realistic improper ferroelectrics, the measured dielectric permittivity in the paraelectric phase region does show some weak temperature dependence. This difference is believed to originate from the assumption that only the first term in the right side of Eq. (S11) is *T*-dependent in the Landau theory of phase transitions.

We now discuss the ferroelectric phase. The inverse dielectric permittivity in the limit of low T ($< T_C$) and low electric field can be obtained:

$$\varepsilon^{-1} = \varepsilon_0^{-1} + 2a_2\eta^2 - \frac{2a_1^2}{(\beta + 2\gamma\eta^2)(1 + 2a_2\chi_0\eta^2)^2} \quad ,$$

(S14)

where $\eta(T)$ is determined by equation:

$$\alpha(T - T_0) + \beta\eta^2 + \gamma\eta^4 - \frac{2a_1^2\chi_0\eta^2}{1 + 2a_2\chi_0\eta^2} + \frac{2a_1^2 a_2\chi_0^2\eta^4}{\left(1 + 2a_2\chi_0\eta^2\right)^2} = 0 \quad ,$$

(S15)

For the present improper ferroelectric, it is clear that the paraelectric to ferroelectric phase transition is of the first-order, indicating the abrupt jump of the dielectric permittivity at T_C. Since $a_2 > 0$, the *T*-dependence of η is:

$$\eta^2 = \frac{2}{3}\Delta\eta^2\left[1 + \left(\frac{T_1 - T}{T_1 - T_0}\right)^{1/2}\right] \quad ,$$

(S16)

where $\Delta\eta^2$ is the jump of η^2 at T_C. Here T_1 is defined by $T_1 = (4T_C - T_0)/3$.

Substituting Eq.(S16) into Eq.(S14), ignoring the last term on the right side of Eq.(S14) results in the dielectric permittivity in the ferroelectric phase:

$$\varepsilon^{-1} = \varepsilon_0^{-1} + \frac{2}{3}\Delta\varepsilon^{-1}[1+(\frac{T_1 - T}{T_1 - T_0})^{1/2}]$$
$$\Delta\varepsilon^{-1} = 2a_2\Delta\eta^2 \quad ,$$

(S17)

It is clear that the dielectric permittivity will increase with increasing T in the ferroelectric phase region, and a jump of ε at T_C up to a larger value will occur, as observed for most improper ferroelectrics (*48-50*).

Eq. (S17) is then used to fit the measured dielectric permittivity as a function of T below T_C, while the dielectric permittivity at $T > T_C$ would be a constant.

f (kHz)	T_C (K)	T_1 (K)	T_0 (K)	ε_0^{-1}	$\Delta\varepsilon^{-1}$
5	400.175	400.47	399.29	0.002	0.01313
10	399.85	400.57	397.68	0.0042	0.02007
100	400.58	401.55	393.64	0.0125	0.03049
1000	399.2	401.5	392.3	0.017	0.03358

Optical properties

As shown in Fig. S16, strong PL emission at ~650 nm can be seen under ultraviolet excitation. The strong PL has a quantum efficient of 92% and long lifetime of ~1 ms, as shown in Fig. S17 and S18. Such strong PL is believed to originate from Mn^{2+} ion in an octahedral crystal field, similar to the previous reported hybrid ferroelectrics (*21*). In Fig. S16, the absorption spectrum of TMCM-$MnCl_3$ displays six (groups of) peaks corresponding to electronic transitions between the ground and the excited states of the Mn^{2+} ion in an octahedral crystal field (*51*). Therefore, the photoluminescence mechanism can be ascribed to the transition between the ground state of the *d*-electron configuration $(t_{2g})^3(e_g)^2$ to the upper state of the configuration $(t_{2g})^4(e_g)$ (*52, 53*).

Characterization on thin-film sample of TMCM-MnCl3

The as-prepared thin-film of TMCM-$MnCl_3$ shows very good coverage and appears very uniform under optical microscopy, as shown in Fig. S19. Similar lamellar shaped domain structures were also observed on thin-film in poly-domain state, as shown in Fig. S20. To confirm the ferroelectricity in such thin-film, a local PFM spectroscopy was carried out. By applying different bias DC voltage, the amplitude and phase signal of piezoresponse were recorded as functions of bias DC voltage, as shown in Fig. S21. The hysteresis phase loop and butterfly amplitude curve are typical evidence for polarization reversal. To further visualize such polarization reversal process, following the same method for bulk sample, DC bias voltage was applied on thin-film surface to manipulate the local polarization states, and PFM phase images were obtained before and after the polarization manipulation

as shown in Fig. S22. The macroscopic ferroelectricity was also confirmed by double-wave method, as shown in Fig. S23.

$Me_3NCH_2ClCdCl_3$ ($TMCM\text{-}CdCl_3$)

By replacing the Mn in $TMCM\text{-}MnCl_3$ to Cd, one obtains another molecular ferroelectric compound of $Me_3NCH_2ClCdCl_3$ ($TMCM\text{-}CdCl_3$), which has identical structure and properties to $TMCM\text{-}MnCl_3$. The structure of $TMCM\text{-}CdCl_3$ in HTP and LTP are illustrated in Fig. S24 and Fig. S25. The d_{33} of $TMCM\text{-}CdCl_3$ is measured to be 220-240 pC/N, even larger than that of $TMCM\text{-}MnCl_3$. The macroscopic piezoelectric coefficient of d_{33} was measured by Berlincourt method as a function of temperature in Fig. S26. The temperature-dependent dielectric permittivity and pyroelectric are also included in Fig. S27A. The ferroelectric polarization of $TMCM\text{-}CdCl_3$ is ~ 6 μC/cm^2 obtained by Sawyer-Tower method (Fig. S27C) and the Curie temperature is ~400 K extracted from DSC (Fig. S27B) and temperature-dependent SHG (Fig. S27D).

Crystal data for $TMCM\text{-}CdCl_3$ at 293 K: $C_4H_{11}CdCl_4N$, Mr = 327.34, monoclinic, Cc, a = 9.4779(19), b = 15.777(3), c = 6.7898(14) Å, V = 1012.1(4) Å^3, Z = 4, D_c = 2.148 g cm^{-3}, μ = 3.148 mm^{-1}, R_1 ($I > 2\sigma(I)$) = 0.0246, wR_2 (all data) = 0.0593, S = 1.034.

At 413 K: $C_4H_{11}CdCl_4N$, Mr = 327.34, hexagonal, $P6_3/mmc$, a = 9.492(9), c = 6.849(11) Å, V = 534.4(14) Å^3, Z = 2, D_c = 2.034 g cm^{-3}, μ = 2.981 mm^{-1}, R_1 ($I > 2\sigma(I)$) = 0.0726, wR_2 (all data) = 0.1869, S = 1.363.

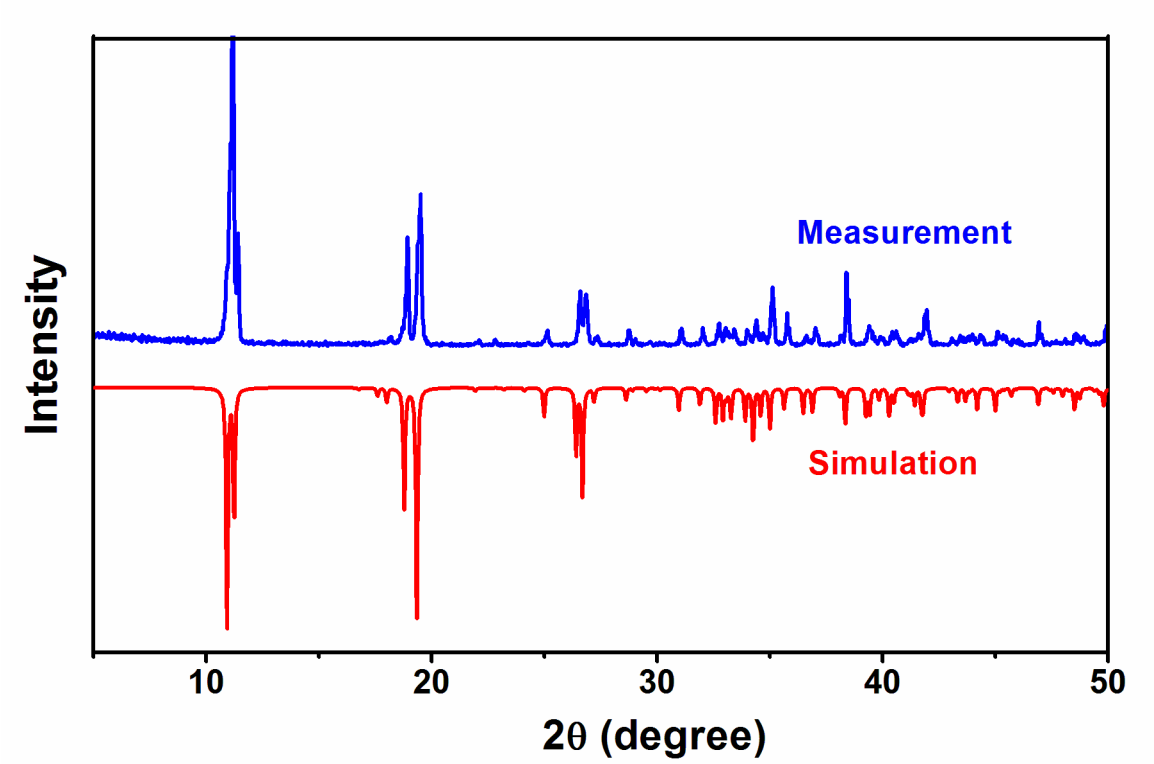


Fig. S1.

Pattern of the powder X-ray diffraction (PXRD) of TMCM-$MnCl_3$, verifying the purity of the bulk phase.

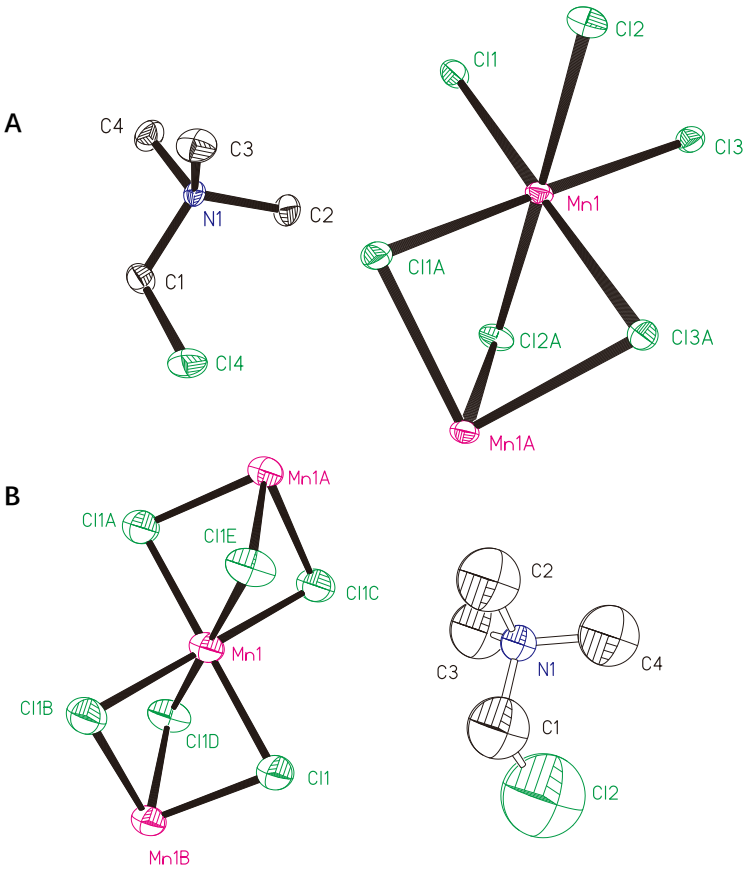


Fig. S2

Ellipsoid drawings of the asymmetric units of the LTP (A) and HTP (B) of TMCM-$MnCl_3$**.** Displacement ellipsoids were drawn at the 30% probability level. Atoms with suffix A–E were generated by symmetry operation. H atoms were omitted for clarity.

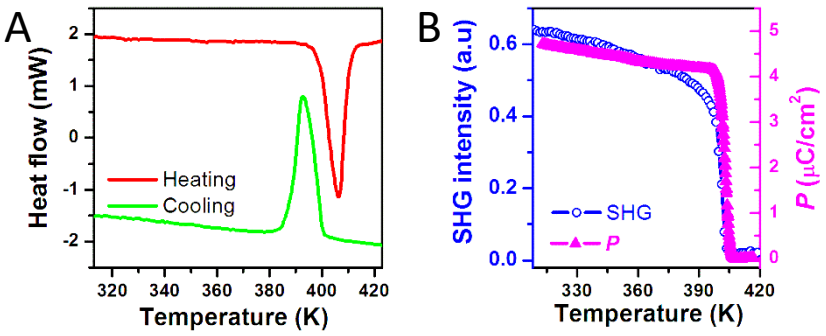


Fig. S3

Temperature-dependent characterization on TMCM-$MnCl_3$. (A) DSC curves in the heating and cooling runs. (B) Temperature-dependent second harmonic generation (blue) and polarization measured by pyroelectric effect (purple).

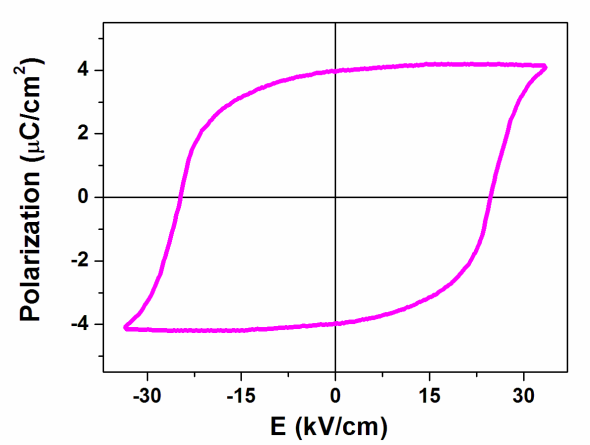


Fig. S4

P-E loop obtained by Sawyer-Tower method on TMCM-$MnCl_3$. A bulk crystal of TMCM-$MnCl_3$ with thickness of ~0.3 mm was used with conducting silver-paste served as top and bottom electrodes. The operation frequency was 50 Hz.

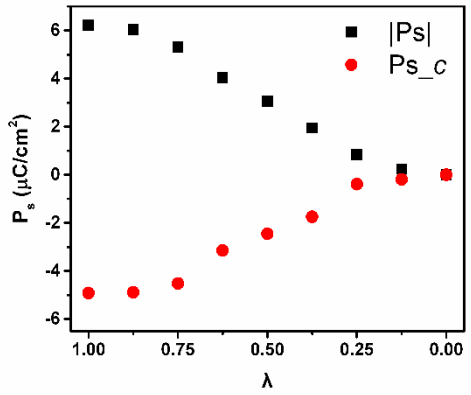


Fig. S5

Calculated polarization of TMCM-$MnCl_3$ as a function of dimensionless parameter λ.

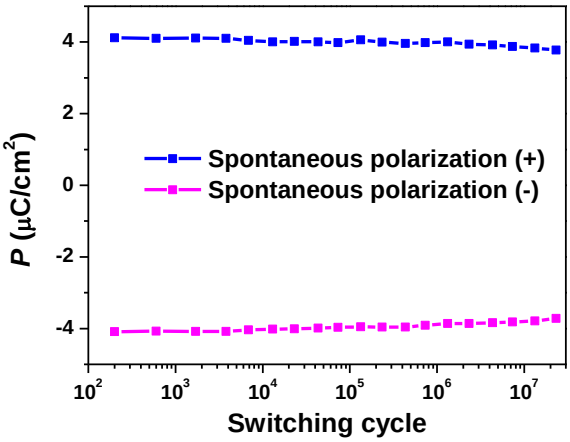


Fig. S6

Fatigue test of ferroelectric polarization of TMCM-$MnCl_3$. The polarization was obtained using Sawyer-Tower method. After 10^7 cycles of polarization reversal, the tested sample exhibited degradation of less than 10%.

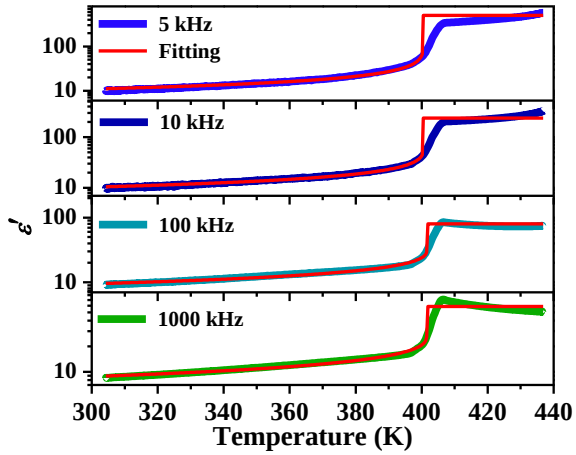


Fig. S7

Fitting of the temperature-dependent real part of dielectric permittivity (ε') of TMCM-$MnCl_3$.

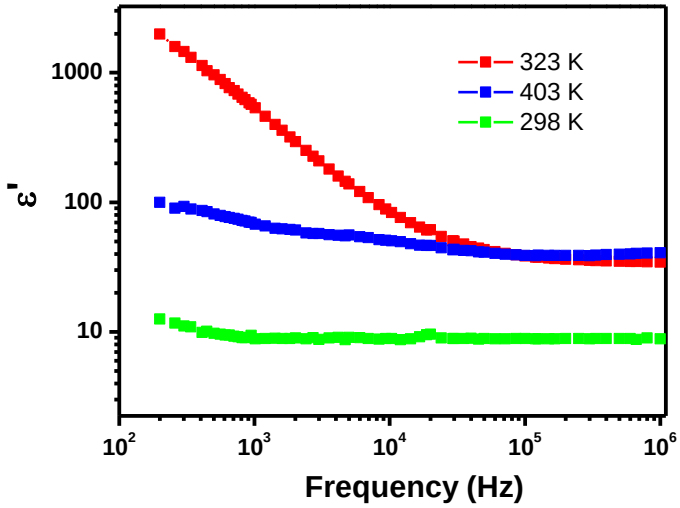


Fig. S8

Real permittivity of TMCM-$MnCl_3$ as a function of frequency at different temperature.

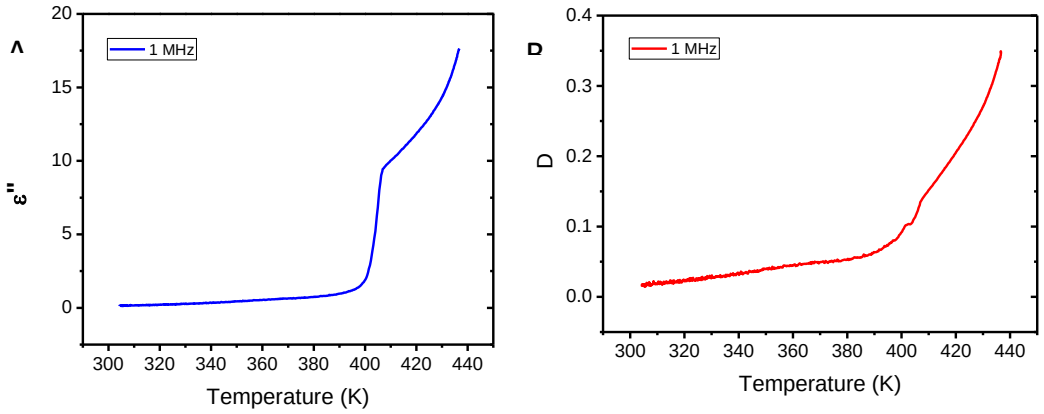


Fig. S9

Imaginary part of dielectric permittivity (ε″) and loss factor $D = \frac{\varepsilon''}{\varepsilon'}$ of TMCM-$MnCl_3$ as a function of temperature at 1 MHz.

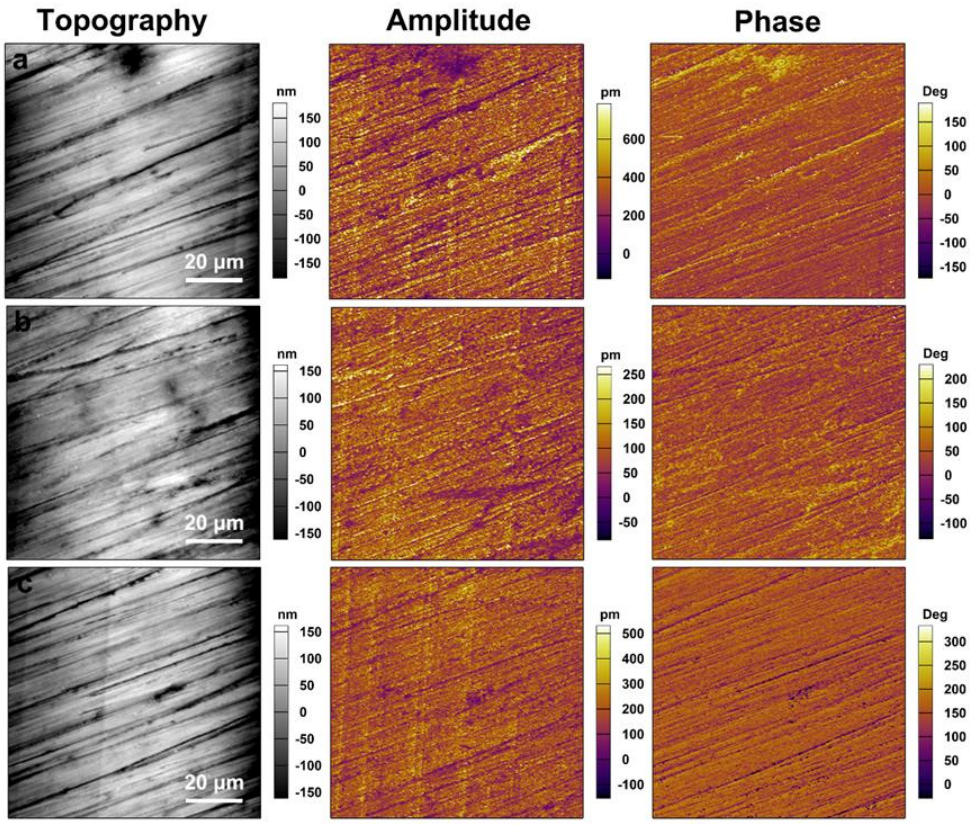


Fig. S10

AFM and PFM images constructed by out-of-plane component of phase and amplitude on randomly selected areas on the as-grown crystal of TMCM-$MnCl_3$. Images in the same row were collected at the same area. The left, middle and right columns of images are constructed by morphology, PFM amplitude and phase, respectively. Those images suggested the as-grown crystals are in the mono-domain state.

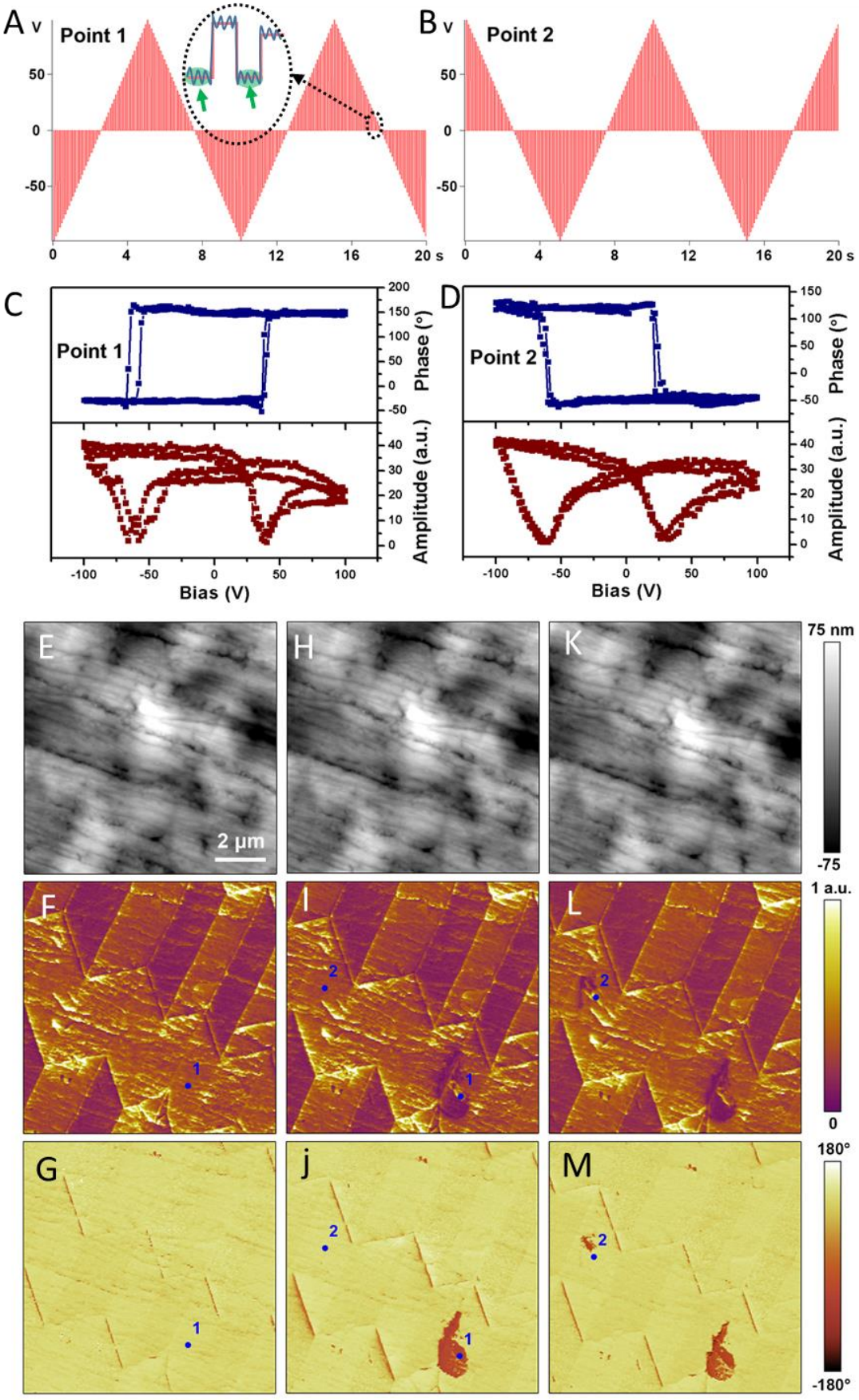

A
V
Point 1
50
0
-50
0
4
8
12
16
20 s
B
V
Point 2
50
0
-50
0
4
8
12
16
20 s
C
Point 1
Phase (°)
Amplitude (a.u.)
Bias (V)
D
Point 2
Phase (°)
Amplitude (a.u.)
Bias (V)
E
H
K
2 µm
75 nm
-75
F
I
L
1 a.u.
0
G
j
M
180°
-180°

Fig. S11

Domain images before and after PFM hysteresis measurement on TMCM-$MnCl_3$. In the hysteresis measurement, an AC drive voltage of 1 V is carried by a stepped DC bias voltage during the switching process, as illustrated in the inset of (A). In order to minimized the electrostatic effect, the piezoresponse induced by V_{AC} is recorded after each step when $V_{DC} = 0$, as indicated by the green arrow in the inset of (A). A 10 × 10 μm area was imaged by OP-PFM before the hysteresis measurement, the corresponding morphology, amplitude and phase images shown in (E), (F) and (G), respectively. On both point 1 and 2, whose positions were indicated in the phase images (G), (J) and (M), a bias V_{DC} was applied on the conductive tip with sawtooth-like waveforms shown in (A) and (B). On point 1, The V_{DC} was swept from -100 V to +100 V and then swept back to -100 V in a duration of 40 s. After the first hysteresis test, the same area was imaged again by PFM, and corresponding images are shown in (H), (I) and (J), respectively. Because the V_{DC} ends at -100 V, the polarization direction of point 1 was switched upward, which is opposite to the initial polarization direction. In phase image (J), an irregular shaped domain with opposite polarization direction can be observed at point 1. Then the tip was moved to point 2 and a V_{DC} in the form of (B) was applied. To compare, waveform of V_{DC} on point 2 had an inverted shape of that of point 1. As a result, the domain structure after second hysteresis test, as shown in (K)-(M), appear slightly different from those obtained after the first hysteresis test. Since the sweep of V_{DC} in (B) ends at +100 V, the corresponding area under the tip was switched back to upward polarization. But due to the diffusive movement of domain wall during the hysteresis test, part of the domain which was away from point 2, was not switched back to its initial state.

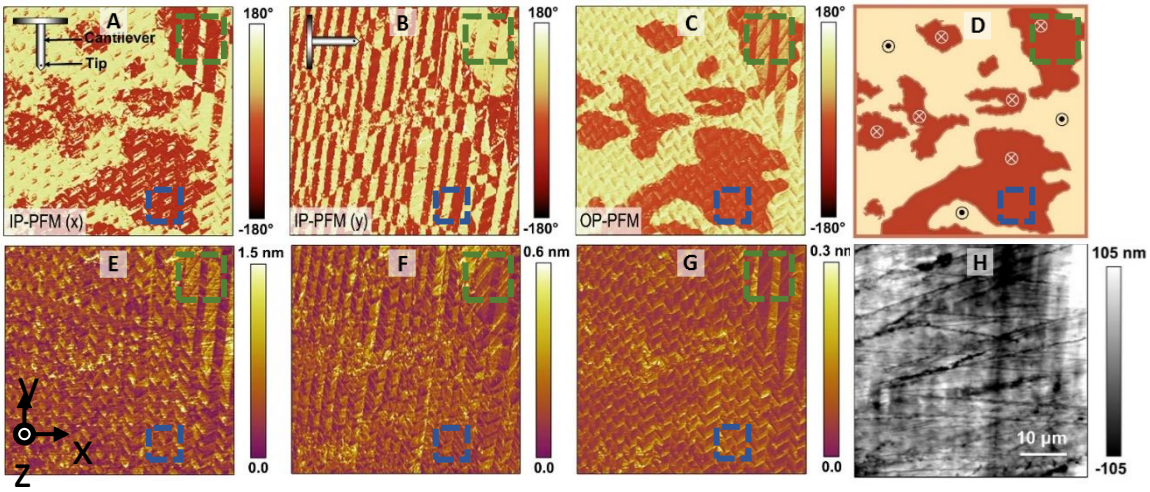


Fig. S12

Large-area PFM images obtained on the crystal of TMCM-$MnCl_3$. (A) and (E) In-plane PFM images constructed by the phase and amplitude of local piezoresponse in x-direction, respectively. (B) and (F) In-plane PFM images constructed by the phase and amplitude of local piezoresponse in y-direction, respectively. (C) and (G) Out-of-plane PFM images constructed by the phase and amplitude of local piezoresponse in z-direction, respectively. Super-domains with 180^o polarization reversal are illustrated in different color contrast in (D). (H) Surface morphology image obtained in the exact same area. The green and blue dashed boxes indicate areas where high-resolution PFM and polarization analysis were carried out, as shown in Fig. S12.

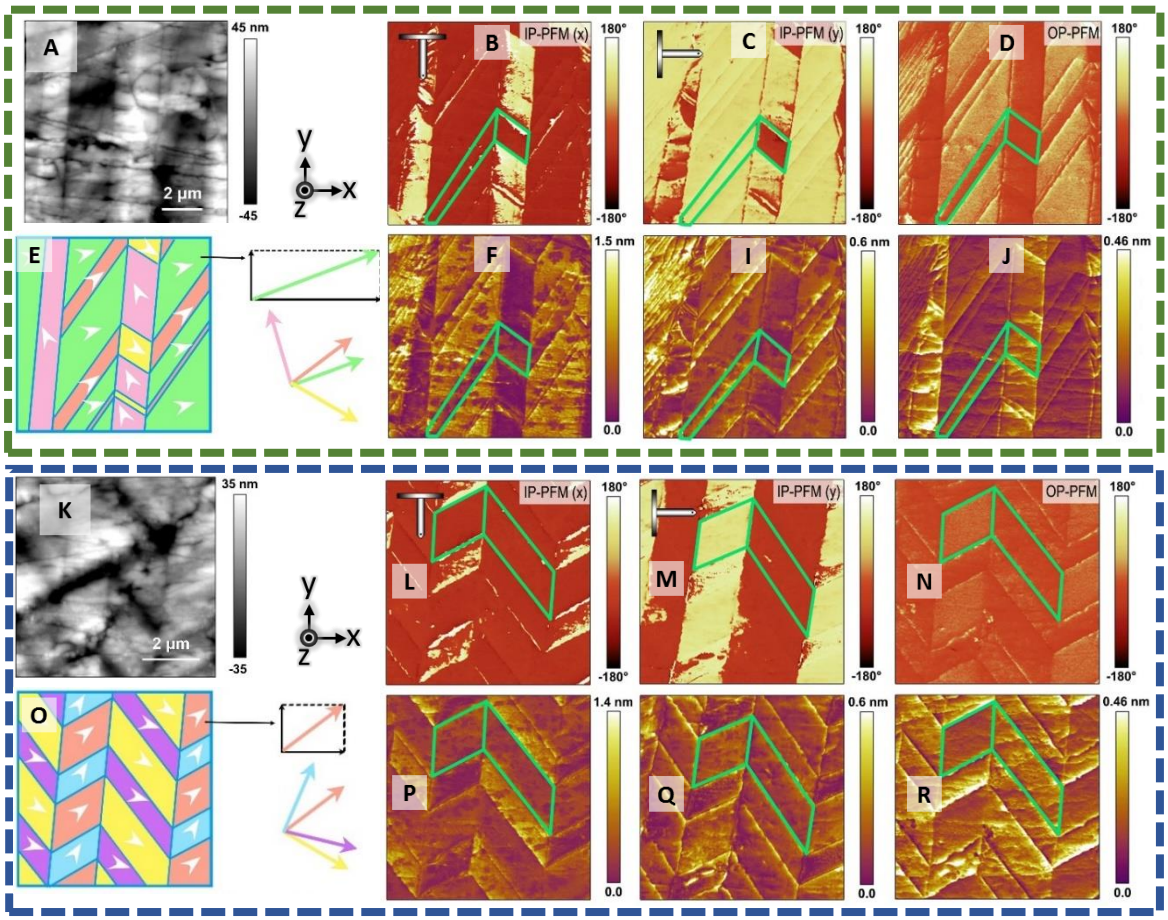


Fig. S13

High-resolution PFM studies of selected areas indicated by green (A-J) and blue (K-R) dashed boxes marked in Fig. S10. (A) The AFM height image of the green boxed area in Fig. S10. Sub-images (B-D) are constructed by phase signal of *x*-, *y*- and *z*-direction components, respectively. Sub-images (F-J) are constructed by amplitude signal of *x*-, *y*- and *z*-direction components, respectively. (E) Illustration of the local domain structures, different color codes mark the domain with same polarization direction. The white arrows indicate the polarization directions in *xy*-plane. Each in-plane polarization direction is estimated by combining the polarization vectors in both *x*- and *y*-directions, as illustrated in the top-right corner of (E), in which the magnitude is determined by averaging the PFM amplitude values over the same domain and direction is determined by phase image. Totally four in-plane polarization directions can be extracted in the green boxed area marked by different colors, as illustrated in bottom-right corner of (E). (K-R) Data obtained in blue dashed box in Fig. S10 are arranged in the same manner as respect to (A-J). Another four in-plane polarization directions can also be extracted in the blue boxed area, as illustrated in bottom-right corner of (O).

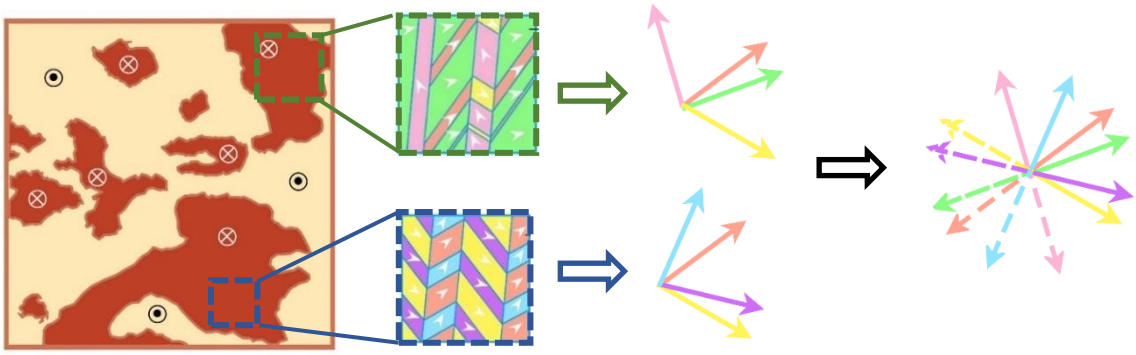


Fig. S14

Combining results from Fig. S9 and Fig. S10, in green and blue dashed areas, each contains four different types of domains with distinct polarization directions. Among them, yellow and orange colored domains have the same polarization directions, which makes total six in-plane polarization directions. Considering the existence of 180^{o} inversion super-domain (six dashed arrows), we found twelve distinct polarization directions, corresponding well with previous discussion about multi-polar-axis and the number of polarization states of TMCM-$MnCl_3$.

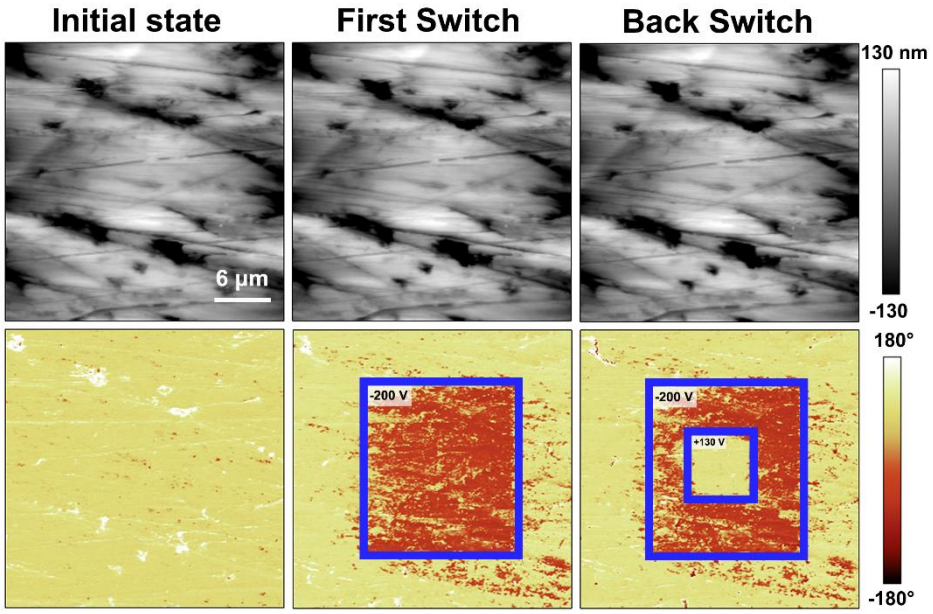


Fig. S15

Local polarization reversal of TMCM-$MnCl_3$ using PFM. The top row was AFM images showing the sample morphology. The bottom row was images constructed by out-of-plane phase signal indicating the polarization direction. In the initial state, PFM phase image showed a nice mono-domain area on the as-grown crystal surface. By applying -200 V DC bias on the tip, the polarization direction in the blue box was reversed indicated by the phase contrast in the middle bottom image.

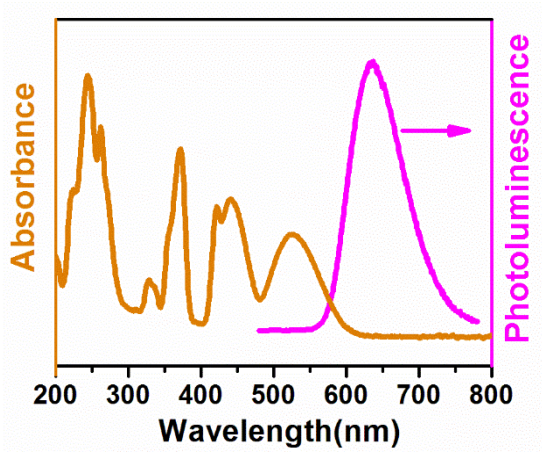


Fig. S16

Comparison of optical absorption (yellow) and emission (purple) spectra of TMCM-$MnCl_3$. There are six (groups of) absorption peaks corresponding to electronic transitions between the ground and the excited states of the Mn^{2+} ion in an octahedral crystal field (*51*). Therefore, the photoluminescence mechanism can be ascribed to the transition between the ground state of the *d*-electron configuration $(t_{2g})^3(e_g)^2$ to the upper state of the configuration $(t_{2g})^4(e_g)$ (*52*, *53*).

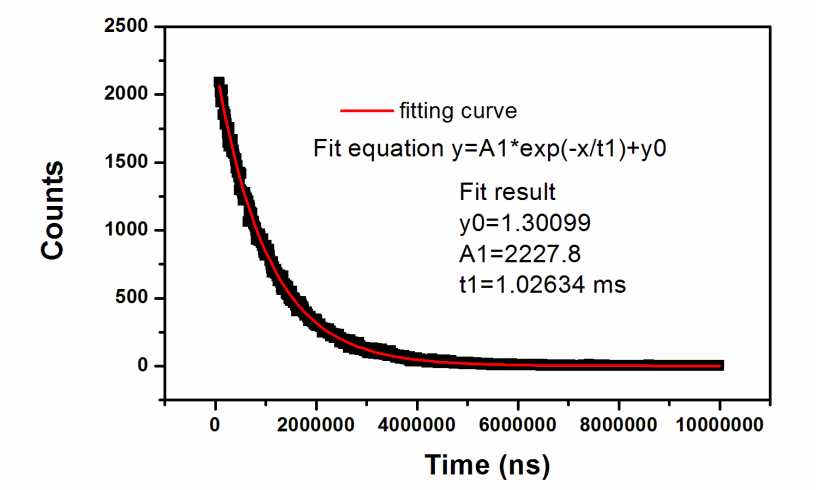


Fig. S17

The lifetime measurement of TMCM-$MnCl_3$, showing a lifetime of 1.0 ms.

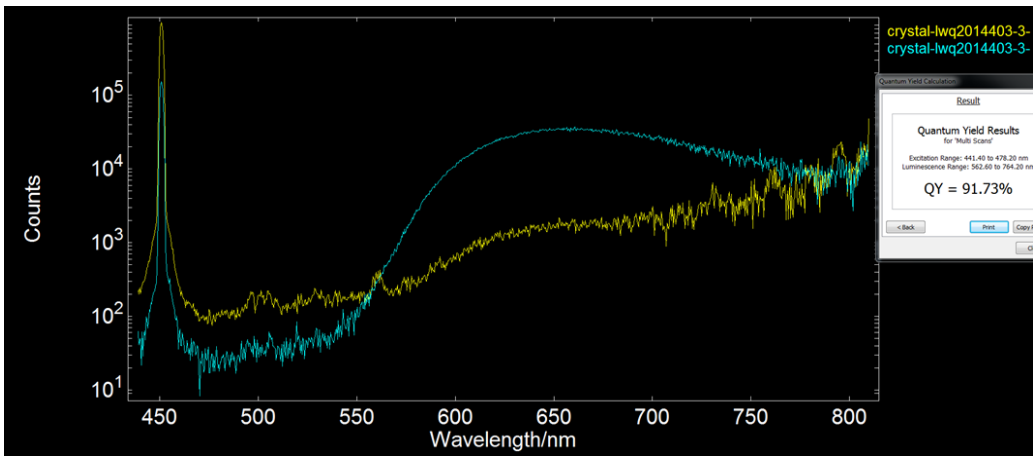


Fig. S18

The quantum yield measurement of TMCM-$MnCl_3$.

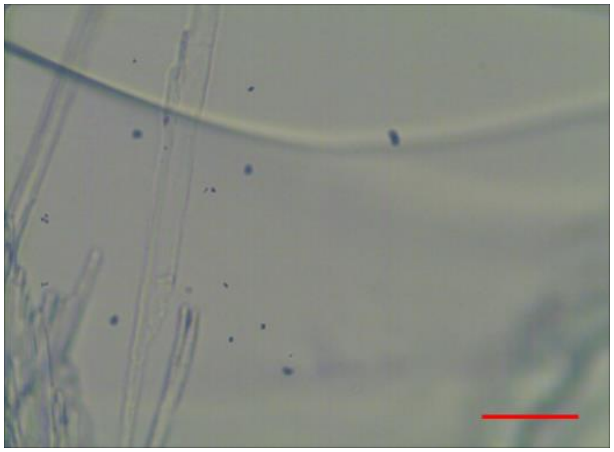


Fig. S19

Optical images of thin-film of TMCM-$MnCl_3$, showing good uniformity under bright-field illumination. (Scale bar: 20 μm)

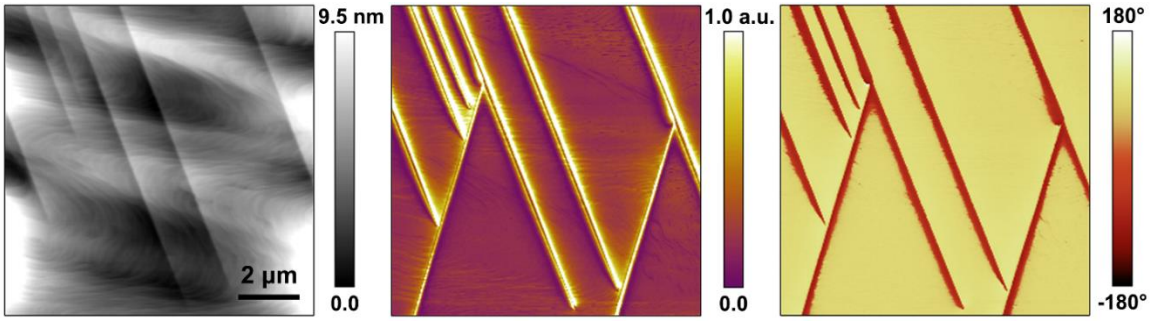


Fig. S20

AFM and PFM images constructed by height (left), out-of-plane amplitude (middle) and out-of-plane phase (right) signal on thin-film sample of TMCM-$MnCl_3$. The lamellar shaped domain structures can be clearly seen.

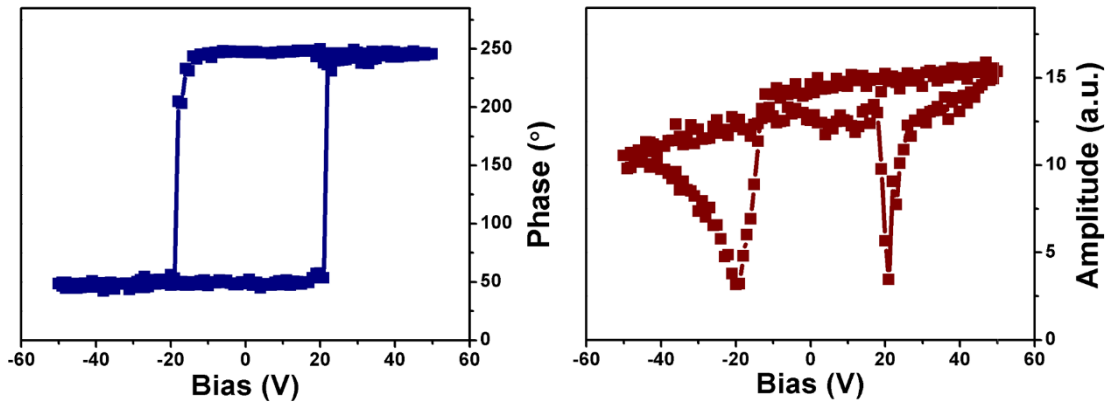


Fig. S21

Local PFM spectroscopy on thin-film sample of TMCM-$MnCl_3$. The out-of-plane PFM phase (left) and amplitude (right) hysteresis loops as functions of DC bias voltage.

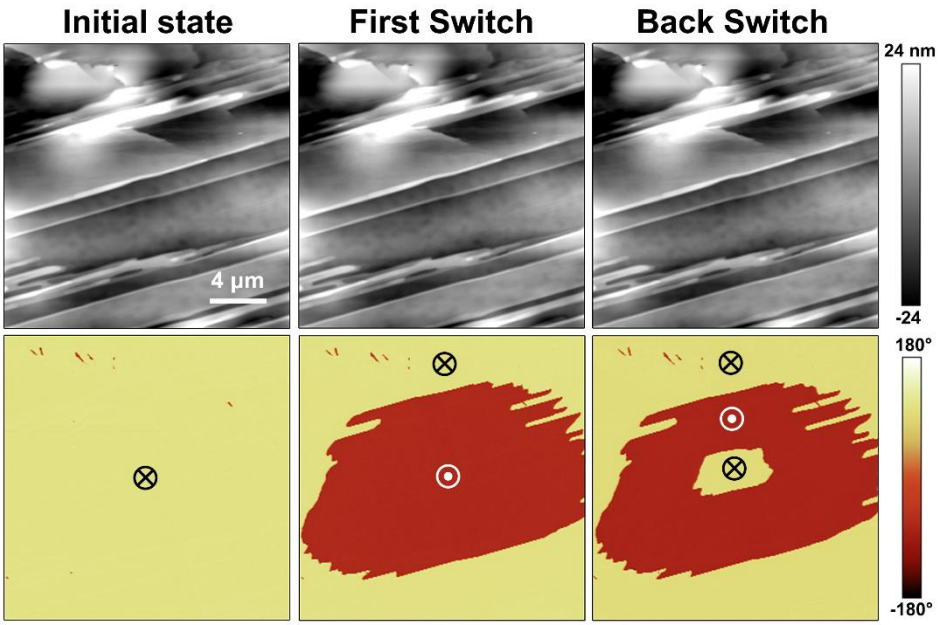


Fig. S22

The out-of-plane PFM images show ferroelectric polarization switching process. Topography (top) and phase (bottom) images for the 20 × 20 µm^2 area of the thin film of TMCM-$MnCl_3$, which were taken (a) in mono-domain state, after applying tip biases of (b) -26 V and (c) after subsequently applying +28 V in the central region. The direction of the polarization is indicated by color contrast.

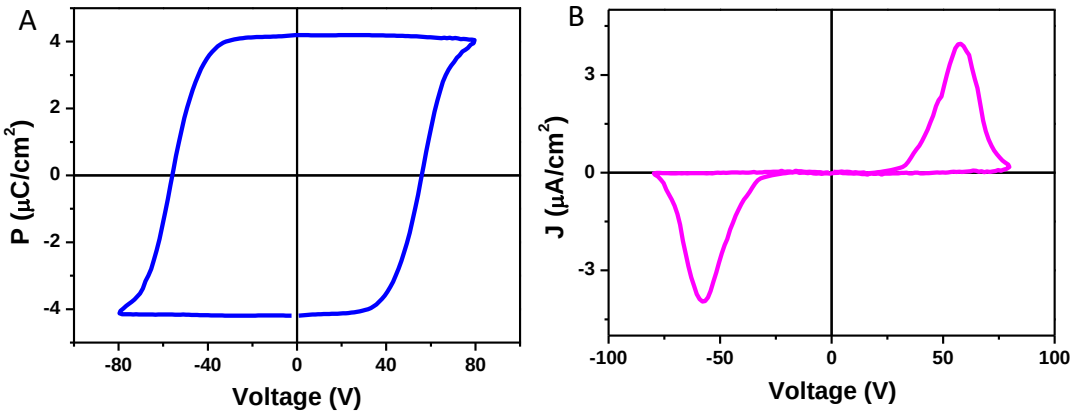


Fig. S23

(A) Current density-filed (*J*~*V*) curves and (B) polarization-electric field (*P*~*E*) hysteresis loop obtained on thin-film sample of TMCM-$MnCl_3$.

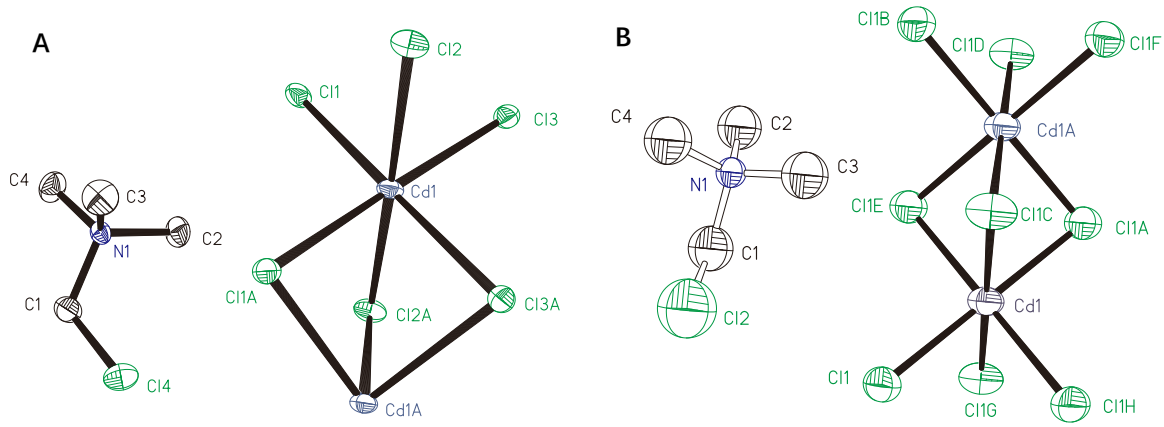


Fig. S24

Ellipsoid drawings of the asymmetric units of the LTP (A) and HTP (B) of TMCM-$CdCl_3$. Displacement ellipsoids were drawn at the 30% probability level. Atoms with suffix A–E were generated by symmetry operation. H atoms were omitted for clarity.

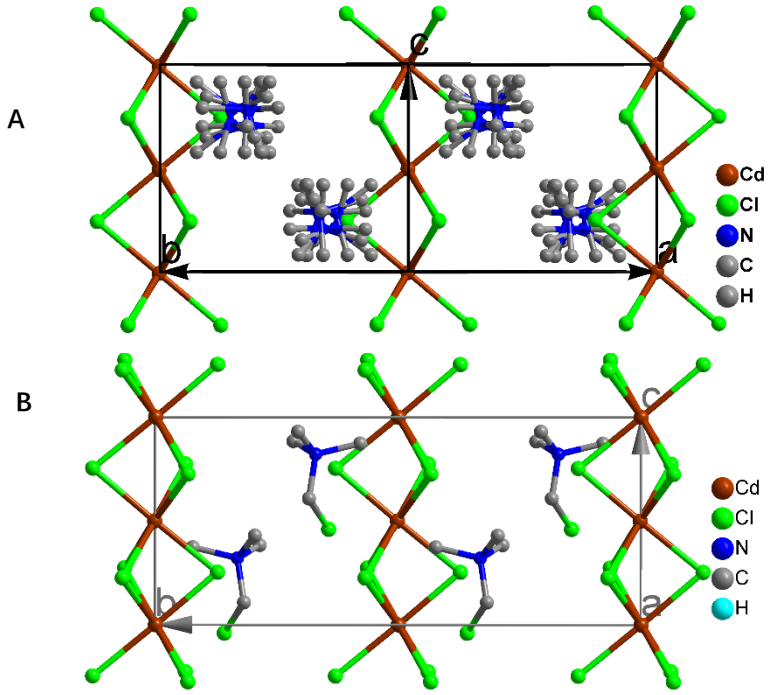


Fig. S25

The packing view of TMCM-$CdCl_3$ in the HTP (A) and the LTP (B).

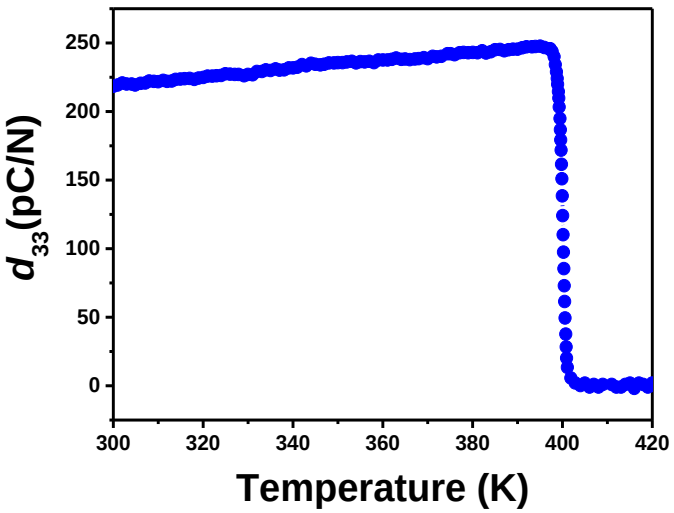


Fig. S26

Temperature dependent d_{33} of TMCM-$CdCl_3$ measured by Berlincourt method.

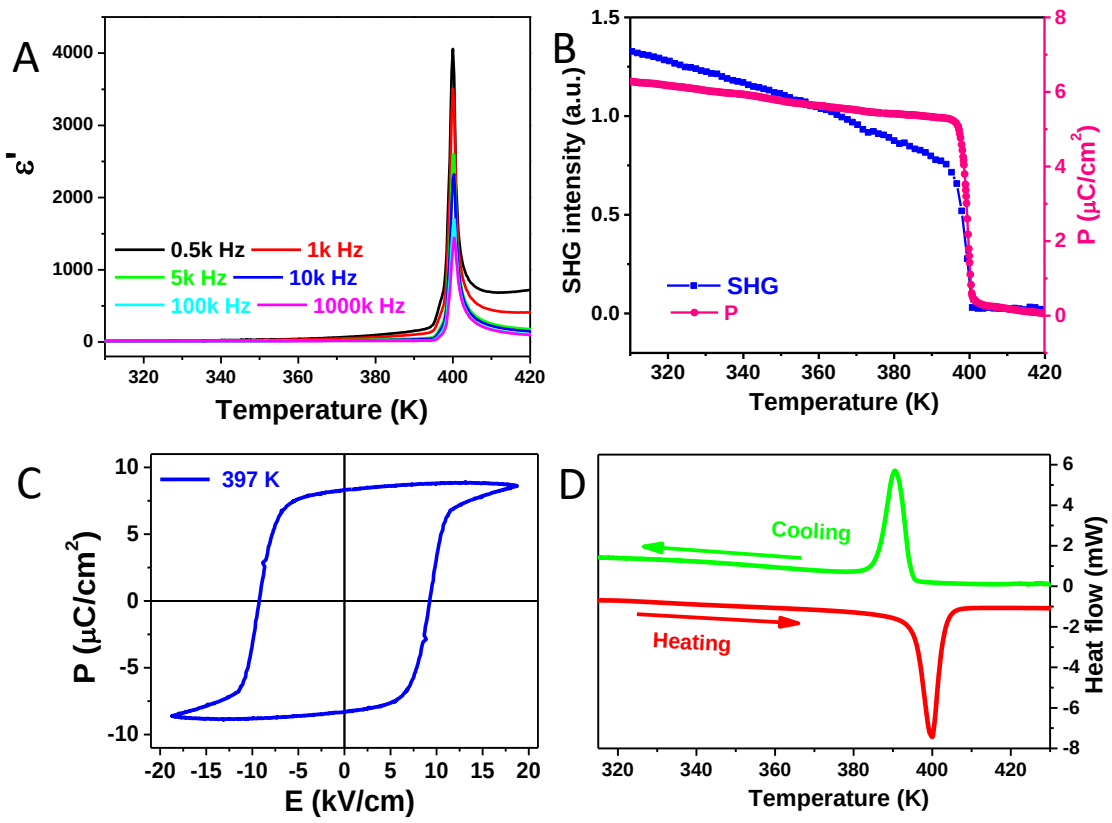


Fig. S27

Characterization data of TMCM-$CdCl_3$. (A) Temperature dependent of the real part of dielectric permittivity (ε′). (B) Temperature dependent results of SHG and pyroelectric response. (C) polarization-electric field (*P*~*E*) hysteresis loops. (C) DSC curves of cooling and heating of TMCM-$CdCl_3$.

Table S1.

Lattice parameter of TMCM-$MnCl_3$ in LTP and HTP.

	LTP	HTP
Temperature (K)	293	423
Crystal system, space group	Monoclinic *Cc*	Hexagonal $P6_3/mmc$
a (Å)	9.478(5)	9.523(5)
b (Å)	15.741(8)	9.523(5)
c (Å)	6.577(3)	6.638(7)
α(degree)	90	90
β (degree)	94.838(7)	90
γ(degree)	90	120

Table S2.

List of d_{33} measured value on different samples and comparison to reported value.

Piezoelectrics	*Measured direction*	*Measured* d_{33} (pC/N)*	*Reference* d_{33} (pC/N)	Source
PZT ($Pb(Zr_{0.52}Ti_{0.48})O_3$)	Ceramic (Poling)	265	220[54]	Prepared by ourselves according to the literature[1]
$BaTiO_3$ (poling)	*c*-aixs**	105	85~95[55]	Purchased from Hefei Ke Jing Materials Technology Co., Ltd. http://www.kjmti.com/
$BaTiO_3$ (no poling)	*c*-aixs	10	> 0 [56]	
PVDF (110 μm)	Thin film	30	22~33[57, 58]	Purchased from MEAS, USA http://www.te.com/usa-en/products/families/meas.html
TGS	*b*-aixs	22	23[59]	Prepared by ourselves according to the literature[7]
DIPAB	*b*-aixs	11	11[10]	Prepared by ourselves according to the literature[8]
$LiNbO_3$	*c*-aixs	11	6~16[60]	Purchased from Hefei Ke Jing Materials Technology Co., Ltd. http://www.kjmti.com/
Rochelle salt	*a*-aixs	7	3~25[61]	Prepared by ourselves according to the literature [11]
KTP	*b*-aixs	6	6.1[62]	Purchased from Fujian CASTECH Crystals, Inc. http://www.castech.com/
Croconic acid	*c*-aixs	5	N/A	Prepared by ourselves according to the literature [12]
ZnO	*c*-aixs	3	2.3~3.5[63]	Purchased from Hefei Ke Jing Materials Technology Co., Ltd. http://www.kjmti.com/
Nylon***	Thin film	2	2[64]	Purchased from ARKEMA, France http://www.arkema.com/en/
TMCM-$MnCl_3$	*c*-aixs	185	This work	This work
TMCM-$CdCl_3$	c-aixs	220	This work	This work

* All measurement was done in our lab using d_{33} meter via Berlincourt method as described in Materials and Methods in Supplementary Materials. All measurement were carried out at room temperature, except for Rochelle salt which was studied at ~283 K.

** d_{33} of single crystalline BTO along [111] is reported to be ≥190 pC/N (*14, 15*).

*** Nylon-11

Table S3.

Calculated ferroelectric polarization of TMCM-$MnCl_3$ with different vdW corrections.

vdW correction	experimental structure		optimized structure	
	$\|P_s\|$ μC/cm^2	P_s_*c* μC/cm^2	$\|P_s\|$ μC/cm^2	P_s_*c* μC/cm^2
DFT-D2[45]	5.74	-4.48	6.21	-4.92
DFT-D3[65]	5.74	-4.48	6.00	-4.63
optPBE[66-68]	5.80	-4.52	5.98	-4.75
optB88[66-68]	5.80	-4.52	5.98	-4.76
optB86b[66-68]	5.80	-4.52	5.98	-4.76
DF2- rPW86[66-68]	5.81	-4.53	5.96	-4.72

References and Notes

1. J. Curie, P. Curie, *C. R. Acad. Sci. Paris* **91**, 294–297 (1880).

2. Materials, methods, and supplementary text are available as supplementary materials.

3. J. Valasek, Piezo-electric and allied phenomena in Rochelle salt. *Phys. Rev.* **17**, 475–481 (1921). doi:10.1103/PhysRev.17.475

4. J. Rödel *et al*., Perspective on the development of lead-free piezoceramics. *J. Am. Ceram. Soc.* **92**, 1153–1177 (2009).

5. Y. Saito, H. Takao, T. Tani, T. Nonoyama, K. Takatori, T. Homma, T. Nagaya, M. Nakamura, Lead-free piezoceramics. *Nature* **432**, 84–87 (2004). doi:10.1038/nature03028 Medline

6. Z. L. Wang, J. Song, Piezoelectric nanogenerators based on zinc oxide nanowire arrays. *Science* **312**, 242–246 (2006). doi:10.1126/science.1124005 Medline

7. T. Akutagawa, H. Koshinaka, D. Sato, S. Takeda, S. Noro, H. Takahashi, R. Kumai, Y. Tokura, T. Nakamura, Ferroelectricity and polarity control in solid-state flip-flop supramolecular rotators. *Nat. Mater.* **8**, 342–347 (2009). doi:10.1038/nmat2377 Medline

8. B. Xu, S. Ren, Integrated charge transfer in organic ferroelectrics for flexible multisensing materials. *Small* **12**, 4502–4507 (2016). doi:10.1002/smll.201600980 Medline

9. P.-P. Shi, Y.-Y. Tang, P.-F. Li, W.-Q. Liao, Z.-X. Wang, Q. Ye, R.-G. Xiong, Symmetry breaking in molecular ferroelectrics. *Chem. Soc. Rev.* **45**, 3811–3827 (2016). doi:10.1039/C5CS00308C Medline

10. D. W. Fu, H.-L. Cai, Y. Liu, Q. Ye, W. Zhang, Y. Zhang, X.-Y. Chen, G. Giovannetti, M. Capone, J. Li, R.-G. Xiong, Diisopropylammonium bromide is a high-temperature molecular ferroelectric crystal. *Science* **339**, 425–428 (2013). doi:10.1126/science.1229675 Medline

11. A. S. Tayi, A. K. Shveyd, A. C.-H. Sue, J. M. Szarko, B. S. Rolczynski, D. Cao, T. J. Kennedy, A. A. Sarjeant, C. L. Stern, W. F. Paxton, W. Wu, S. K. Dey, A. C. Fahrenbach, J. R. Guest, H. Mohseni, L. X. Chen, K. L. Wang, J. F. Stoddart, S. I. Stupp, Room-temperature ferroelectricity in supramolecular networks of charge-transfer complexes. *Nature* **488**, 485–489 (2012). doi:10.1038/nature11395 Medline

12. S. Horiuchi, Y. Tokunaga, G. Giovannetti, S. Picozzi, H. Itoh, R. Shimano, R. Kumai, Y. Tokura, Above-room-temperature ferroelectricity in a single-component molecular crystal. *Nature* **463**, 789–792 (2010). doi:10.1038/nature08731 Medline

13. D. A. Bonnell, Materials science. Ferroelectric organic materials catch up with oxides. *Science* **339**, 401–402 (2013). doi:10.1126/science.1232939 Medline

14. R. Bechmann, Elastic, piezoelectric, and dielectric constants of polarized barium titanate ceramics and some applications of the piezoelectric equations. *J. Acoust. Soc. Am.* **28**, 347–350 (1956). doi:10.1121/1.1908324

15. S. Wada, K. Yako, H. Kakemoto, T. Tsurumi, T. Kiguchi, Enhanced piezoelectric properties of barium titanate single crystals with different engineered-domain sizes. *J. Appl. Phys.* **98**, 014109 (2005). doi:10.1063/1.1957130

16. D. B. Mitzi, C. A. Feild, W. T. A. Harrison, A. M. Guloy, Conducting tin halides with a layered organic-based perovskite structure. *Nature* **369**, 467–469 (1994). doi:10.1038/369467a0

17. H. Cho, S.-H. Jeong, M.-H. Park, Y.-H. Kim, C. Wolf, C.-L. Lee, J. H. Heo, A. Sadhanala, N. Myoung, S. Yoo, S. H. Im, R. H. Friend, T.-W. Lee, Overcoming the electroluminescence efficiency limitations of perovskite light-emitting diodes. *Science* **350**, 1222–1225 (2015). doi:10.1126/science.aad1818 Medline

18. F. Hao, C. C. Stoumpos, D. H. Cao, R. P. H. Chang, M. G. Kanatzidis, Lead-free solid-state organic-inorganic halide perovskite solar cells. *Nat. Photonics* **8**, 489–494 (2014). doi:10.1038/nphoton.2014.82

19. H. Tsai, W. Nie, J.-C. Blancon, C. C. Stoumpos, R. Asadpour, B. Harutyunyan, A. J. Neukirch, R. Verduzco, J. J. Crochet, S. Tretiak, L. Pedesseau, J. Even, M. A. Alam, G. Gupta, J. Lou, P. M. Ajayan, M. J. Bedzyk, M. G. Kanatzidis, A. D. Mohite, High-efficiency two-dimensional Ruddlesden-Popper perovskite solar cells. *Nature* **536**, 312–316 (2016). doi:10.1038/nature18306 Medline

20. H.-Y. Ye, W.-Q. Liao, C.-L. Hu, Y. Zhang, Y.-M. You, J.-G. Mao, P.-F. Li, R.-G. Xiong, Bandgap engineering of lead-halide perovskite-type ferroelectrics. *Adv. Mater.* **28**, 2579–2586 (2016). doi:10.1002/adma.201505224 Medline

21. H.-Y. Ye, Q. Zhou, X. Niu, W.-Q. Liao, D.-W. Fu, Y. Zhang, Y.-M. You, J. Wang, Z.-N. Chen, R.-G. Xiong, High-temperature ferroelectricity and photoluminescence in a hybrid organic-inorganic compound: (3-pyrrolinium)$MnCl_3$. *J. Am. Chem. Soc.* **137**, 13148–13154 (2015). doi:10.1021/jacs.5b08290 Medline

22. K. Aizu, Possible species of ferroelastic crystals and of simultaneously ferroelectric and ferroelastic crystals. *J. Phys. Soc. Jpn.* **27**, 387–396 (1969). doi:10.1143/JPSJ.27.387

23. L. Hu, S. Dalgleish, M. M. Matsushita, H. Yoshikawa, K. Awaga, Storage of an electric field for photocurrent generation in ferroelectric-functionalized organic devices. *Nat. Commun.* **5**, 3279 (2014). doi:10.1038/ncomms4279 Medline

24. W. Zhang, R.-G. Xiong, Ferroelectric metal-organic frameworks. *Chem. Rev.* **112**, 1163–1195 (2012). doi:10.1021/cr200174w Medline

25. A. P. Levanyuk, D. G. Sannikov, Improper ferroelectrics. *Usp. Fiziol. Nauk* **112**, 561–589 (1974). doi:10.3367/UFNr.0112.197404a.0561

26. Y. Zhang, Y. Liu, H. Y. Ye, D. W. Fu, W. Gao, H. Ma, Z. Liu, Y. Liu, W. Zhang, J. Li, G. L. Yuan, R. G. Xiong, A molecular ferroelectric thin film of imidazolium perchlorate that shows superior electromechanical coupling. *Angew. Chem. Int. Ed.* **53**, 5064–5068 (2014). Medline

27. D. Damjanovic, Ferroelectric, dielectric and piezoelectric properties of ferroelectric thin films and ceramics. *Rep. Prog. Phys.* **61**, 1267–1324 (1998). doi:10.1088/0034-4885/61/9/002

28. D. A. Bonnell, S. V. Kalinin, A. Kholkin, A. Gruverman, Piezoresponse force microscopy: A window into electromechanical behavior at the nanoscale. *MRS Bull.* **34**, 648–657 (2009). doi:10.1557/mrs2009.176

29. A. L. Kholkin, S. V. Kalinin, A. Roelofs, A. Gruverman, in *Scanning Probe Microscopy: Electrical and Electromechanical Phenomena at the Nanoscale*, S. Kalinin, A. Gruverman, Eds. (Springer New York, 2007), pp. 173–214.

30. H. Lu, T. Li, S. Poddar, O. Goit, A. Lipatov, A. Sinitskii, S. Ducharme, A. Gruverman, Statics and dynamics of ferroelectric domains in diisopropylammonium bromide. *Adv. Mater.* **27**, 7832–7838 (2015). doi:10.1002/adma.201504019 Medline

31. D. A. Bonnell, D. N. Basov, M. Bode, U. Diebold, S. V. Kalinin, V. Madhavan, L. Novotny, M. Salmeron, U. D. Schwarz, P. S. Weiss, Imaging physical phenomena with local probes: From electrons to photons. *Rev. Mod. Phys.* **84**, 1343–1381 (2012). doi:10.1103/RevModPhys.84.1343

32. M. E. Caspari, W. J. Merz, The electromechanical behavior of $BaTiO_3$ single-domain crystals. *Phys. Rev.* **80**, 1082–1089 (1950). doi:10.1103/PhysRev.80.1082

33. W. Heywang, K. Lubitz, W. Wersing, *Piezoelectricity: Evolution and Future of a Technology* (Springer, 2008).

34. N. Setter, E. L. Colla, *Ferroelectric Ceramics: Tutorial Reviews, Theory, Processing, and Applications* (Birkhauser, 1993).

35. J. L. Jones, M. Hoffman, J. E. Daniels, A. J. Studer, Ferroelastic contribution to the piezoelectric response in lead zirconate titanate by in situ stroboscopic neutron diffraction. *Physica B* **385–386**, 100–102 (2006). doi:10.1016/j.physb.2006.05.115

36. H. Y. Ye, S.-H. Li, Y. Zhang, L. Zhou, F. Deng, R.-G. Xiong, Solid state molecular dynamic investigation of an inclusion ferroelectric: [(2,6-diisopropylanilinium)([18]crown-6)]BF_4. *J. Am. Chem. Soc.* **136**, 10033–10040 (2014). doi:10.1021/ja503344b Medline

37. W. Q. Liao, Y. Zhang, C.-L. Hu, J.-G. Mao, H.-Y. Ye, P.-F. Li, S. D. Huang, R.-G. Xiong, A lead-halide perovskite molecular ferroelectric semiconductor. *Nat. Commun.* **6**, 7338 (2015). doi:10.1038/ncomms8338 Medline

38. R. Xu, S. Liu, I. Grinberg, J. Karthik, A. R. Damodaran, A. M. Rappe, L. W. Martin, Ferroelectric polarization reversal via successive ferroelastic transitions. *Nat. Mater.* **14**, 79–86 (2015). doi:10.1038/nmat4119 Medline

39. T. Liu, K. G. Webber, C. S. Lynch, Finite element analysis with a ferroelectric and ferroelastic material model. *Integr. Ferroelectr.* **101**, 164–173 (2008). doi:10.1080/10584580802470959

40. R. D. King-Smith, D. Vanderbilt, Theory of polarization of crystalline solids. *Phys. Rev. B Condens. Matter* **47**, 1651–1654 (1993). doi:10.1103/PhysRevB.47.1651 Medline

41. D. Vanderbilt, R. D. King-Smith, Electric polarization as a bulk quantity and its relation to surface charge. *Phys. Rev. B Condens. Matter* **48**, 4442–4455 (1993). doi:10.1103/PhysRevB.48.4442 Medline

42. G. Kresse, J. Furthmüller, Efficient iterative schemes for ab initio total-energy calculations using a plane-wave basis set. *Phys. Rev. B Condens. Matter* **54**, 11169–11186 (1996). doi:10.1103/PhysRevB.54.11169 Medline

43. G. Kresse, J. Furthmuller, Efficiency of ab-initio total energy calculations for metals and semiconductors using a plane-wave basis set. *Comput. Mater. Sci.* **6**, 15–50 (1996). doi:10.1016/0927-0256(96)00008-0

44. J. P. Perdew, K. Burke, M. Ernzerhof, Generalized gradient approximation made simple. *Phys. Rev. Lett.* **77**, 3865–3868 (1996). doi:10.1103/PhysRevLett.77.3865 Medline

45. S. Grimme, Semiempirical GGA-type density functional constructed with a long-range dispersion correction. *J. Comput. Chem.* **27**, 1787–1799 (2006). doi:10.1002/jcc.20495 Medline

46. V. Dvořák, Improper Ferroelectrics. *Ferroelectrics* **7**, 1–9 (1974). doi:10.1080/00150197408237942

47. J. Kobayashi, Y. Enomoto, Y. Sato, A phenomenological theory of dielectric and mechanical properties of improper ferroelectric crystals. *Phys. Status Solidi, B Basic Res.* **50**, 335–343 (1972). doi:10.1002/pssb.2220500139

48. A. Shaulov, W. A. Smith, H. Schmid, Dielectric Anomalies in Boracites. *Ferroelectrics* **34**, 219–225 (1981). doi:10.1080/00150198108238728

49. F. Smutný, J. Fousek, Ferroelectric transition in Co-I-boracite. *Phys. Status Solidi, B Basic Res.* **40**, K13–K15 (1970). doi:10.1002/pssb.19700400147

50. H. Schmid, P. Chan, L. A. Petermann, F. Teufel, M. Mandly, Spontaneous polarization, dielectric-constant, dc resistivity, and specific-heat of orthorhombic boracite $Fe_3B_7O_{13}I$. *Ferroelectrics* **13**, 351–352 (1976). doi:10.1080/00150197608236608

51. K. E. Lawson, Optical Studies of Electronic transitions in hexa- and tetracoordinated Mn^{2+} crystals. *J. Chem. Phys.* **47**, 3627–3633 (1967). doi:10.1063/1.1712432

52. L. E. Orgel, Phosphorescence of solids containing the manganous or ferric ions. *J. Chem. Phys.* **23**, 1958 (1955). doi:10.1063/1.1740614

53. L. E. Orgel, Band widths in the spectra of manganous and other transition-metal complexes. *J. Chem. Phys.* **23**, 1824–1826 (1955). doi:10.1063/1.1740585

54. C. A. Randall, N. Kim, J. P. Kucera, W. W. Cao, T. R. Shrout, Intrinsic and extrinsic size effects in fine-grained morphotropic-phase-boundary lead zirconate titanate ceramics. *J. Am. Ceram. Soc.* **81**, 677–688 (1998). doi:10.1111/j.1151-2916.1998.tb02389.x

55. M. Zgonik, P. Bernasconi, M. Duelli, R. Schlesser, P. Günter, M. H. Garrett, D. Rytz, Y. Zhu, X. Wu, Dielectric, elastic, piezoelectric, electro-optic, and elasto-optic tensors of $BaTiO_3$ crystals. *Phys. Rev. B Condens. Matter* **50**, 5941–5949 (1994). doi:10.1103/PhysRevB.50.5941 Medline

56. A. H. Meitzler, H. L. Stadler, Piezoelectric and dielectric characteristics of single-crystal barium titanate plates. *Bell Syst. Tech. J.* **37**, 719–738 (1958). doi:10.1002/j.1538-7305.1958.tb03884.x

57. S. B. Lang, S. Muensit, Review of some lesser-known applications of piezoelectric and pyroelectric polymers. *Appl. Phys., A Mater. Sci. Process.* **85**, 125–134 (2006). doi:10.1007/s00339-006-3688-8

58. P. Ueberschlag, PVDF piezoelectric polymer. *Sens. Rev.* **21**, 118–126 (2001). doi:10.1108/02602280110388315

59. R. G. Xiong, The temperature-dependent domains, SHG effect and piezoelectric coefficient of TGS. *Chin. Chem. Lett.* **24**, 681–684 (2013). doi:10.1016/j.cclet.2013.05.015

60. R. S. Weis, T. K. Gaylord, Lithium-niobate: Summary of physical-properties and crystal-structure. *Appl. Phys., A Mater. Sci. Process.* **37**, 191–203 (1985). doi:10.1007/BF00614817

61. E. Lemaire, R. Moser, C. J. Borsa, H. Shea, D. Briand, Green paper-based piezoelectric material for sensors and actuators. *Procedia Eng.* **120**, 360–363 (2015). doi:10.1016/j.proeng.2015.08.637

62. T. Jungk, A. Hoffmann, E. Soergel, Influence of the inhomogeneous field at the tip on quantitative piezoresponse force microscopy. *Appl. Phys., A Mater. Sci. Process.* **86**, 353–355 (2007). doi:10.1007/s00339-006-3768-9

63. D. A. Scrymgeour, T. L. Sounart, N. C. Simmons, J. W. P. Hsu, Polarity and piezoelectric response of solution grown zinc oxide nanocrystals on silver. *J. Appl. Phys.* **101**, 014316 (2007). doi:10.1063/1.2405014

64. E. K. Akdogan, M. Allahverdi, A. Safari, Piezoelectric composites for sensor and actuator applications. *IEEE Trans. Ultrason. Ferroelectr. Freq. Control* **52**, 746–775 (2005). doi:10.1109/TUFFC.2005.1503962 Medline

65. S. Grimme, J. Antony, S. Ehrlich, H. Krieg, A consistent and accurate ab initio parametrization of density functional dispersion correction (DFT-D) for the 94 elements H-Pu. *J. Chem. Phys.* **132**, 154104 (2010). doi:10.1063/1.3382344 Medline

66. J. Klimeš, D. R. Bowler, A. Michaelides, Chemical accuracy for the van der Waals density functional. *J. Phys. Condens. Matter* **22**, 022201 (2010). doi:10.1088/0953-8984/22/2/022201 Medline

67. K. Lee, É. D. Murray, L. Kong, B. I. Lundqvist, D. C. Langreth, Higher-accuracy van der Waals density functional. *Phys. Rev. B* **82**, 081101 (2010). doi:10.1103/PhysRevB.82.081101

68. J. Klimeš, D. R. Bowler, A. Michaelides, Van der Waals density functionals applied to solids. *Phys. Rev. B* **83**, 195131 (2011). doi:10.1103/PhysRevB.83.195131